Published for SISSA by Springer

Received: *September 12, 2013*
Accepted: *October 2, 2013*
Published: *October 23, 2013*

Two-component dark matter

Subhadittya Bhattacharya,[a] **Aleksandra Drozd,**[b] **Bohdan Grzadkowski**[b] **and Jose Wudka**[a]

[a] *Department of Physics, University of California, Riverside, CA 92521, U.S.A.*

[b] *Faculty of Physics, University of Warsaw, 00-681 Warsaw, Poland*

E-mail: subhaditya.bhattacharya@ucr.edu , aleksandra.drozd@fuw.edu.pl, bohdan.grzadkowski@fuw.edu.pl, jose.wudka@ucr.edu

Abstract: We study an extension of the Standard Model (SM) with two interacting cold Dark Matter (DM) candidates: a neutral Majorana fermion (ν) and a neutral scalar singlet (φ). The scalar φ interacts with the SM through the "Higgs portal" coupling while ν at the tree level interacts only with φ through Yukawa interactions. The relic abundance of ν and φ is found by solving the Boltzmann equations numerically; for the case $m_\nu > m_\varphi$ we also derive a reliable approximate analytical solution. Effects of the interaction between the two DM components are discussed. A scan over the parameter space is performed to determine the regions consistent with the WMAP data for DM relic abundance, and with the XENON100 direct detection limits for the DM-nucleus cross section. We find that although a large region of the parameter space is allowed by the WMAP constraints, the XENON100 data severely restricts the parameter space. Taking into account only amplitudes generated at the tree level one finds three allowed regions for the scalar mass: $m_\varphi \sim 62.5$ GeV (corresponding to the vicinity of the Higgs boson resonance responsible for $\varphi\varphi$ annihilation into SM particles), $m_\varphi \simeq 130 - 140$ GeV and $m_\varphi \gtrsim 3$ TeV. 1-loop induced ν-nucleon scattering has been also calculated and discussed. A possibility of DM direct detection by the CREST-II experiment was considered.

Keywords: Cosmology of Theories beyond the SM, Beyond Standard Model

JHEP10(2013)158

Open Access

doi:10.1007/JHEP10(2013)158

Contents

JHEP10(2013)158

1 Introduction

Dark matter (DM) was first postulated by Oort in 1932 to account for the orbital velocities of stars in the Milky Way, and then adopted by Zwicky in 1933 to explain the orbital velocities of galaxies in clusters. The existence of DM is by now well established [1, 2] though compelling astronomical observations, including recent ones involving Bullet cluster (1E0657-558) [3]. It is also know that DM plays a central role in cosmology, affecting both the evolution of the early universe and structure formation [4–7]. Understanding the properties of DM is one of the great current problems in modern cosmology.

Despite a wealth of observations and many experimental efforts, the nature and composition of DM remains unknown. Since the early 80's there have been continuous attempts to determine whether DM might be associated with one or more elementary particles, an idea that can be probed using both collider experiments as well as cosmological observations. The most promising possibility within this scenario is for DM to be composed of cold non-baryonic particles; in this case current measurements of the anisotropy of the cosmic microwave background (CMB) can be used to estimate the non-baryonic DM density at [8]

$$\Omega_{DM}h^2 = 0.1138 \pm 0.0045 \tag{1.1}$$

where the $\Omega_{DM} = \rho_{DM}/\rho_{\rm crit}$ is the ratio of the DM density over the critical density that corresponds to flat universe, and h is the Hubble constant in units of 100 km/(s.Mpc) (in contrast, the density of visible baryonic matter is much much smaller: $\Omega_b h^2 = 0.02264 \pm 0.00050$) [8].

Unfortunately, all Standard Model (SM) particles are excluded as relevant components of DM [9], so one has to look for extensions of the SM that provide stable (or with a decay time longer than the present age of the Universe), massive, neutral particles that might play this role. An enormous amount of work has been done by theoreticians in this direction, considering many types of models, most of which contain a single particle beyond the SM that is stable and might be considered as a DM candidate.

This, however, may not be the case, so that DM could have a multi-component structure (one should remember that the rich variety of SM matter is responsible only for a fiftieth of the matter density in the Universe), and there have already been some studies of multi-component DM in the literature (see for example, [10–36]. Here we would like to investigate a scenario where DM consists of two species — a singlet scalar (φ) and a singlet neutral *Majorana* fermion (ν) (that we will refer to as a "neutrino"). The scalar DM field in this model interacts with the SM through the Higgs field, while the fermionic DM does not couple directly to the SM. However, the fermionic and scalars DM components do interact, so the model provides a simple 'laboratory' where the interesting issue of interactions between DM components can be studied.

The paper is organized as follows. In section 2 we introduce our specific 2-component DM model and discuss its general properties. Then, in section 3 we derive the Boltzmann equations that govern cosmological evolution of the DM components and we obtain and discuss numerical and approximate analytical solutions. In the subsequent section, section 4, we calculate the present DM density and find the regions in parameter space for which it is consistent with (1.1). In section 5 we derive the constraints on our model derived from the direct detection experiments. Section 6 contains our conclusions. In the appendix A we collect formulae related to scalar and fermion pair annihilation.

2 Minimal scalar-fermion model of DM

Our model contains three new particles, all SM singlets: a real scalar φ, and two *majorana* fermions ν_h and ν (two fermions are required in order to generate non-trivial interactions between the DM components), only *one* of the fermions will contribute to the DM relic density. Though the DM sector can contain particles of any spin, the simplest possibilities correspond to the presence of fermions and scalars.

Since all DM particles are singlets under the SM gauge group, their interaction with the SM will be through terms of the form $\mathcal{O}_{DM}\mathcal{O}_{SM}$, where $\mathcal{O}_{SM}$ is gauge invariant operator composed of SM fields; of all such terms we expect those with the lowest dimension to be the most relevant. Within the SM the lowest-dimensional scalar gauge invariant operator is $H^\dagger H$, where H denotes the scalar isodoublet. Restricting ourselves to renormalizable interactions, and assuming that all DM particles transform non-trivially under a symmetry group, fixes the leading $\mathcal{O}_{DM}$ to be of the form φ^2. Therefore, the φ interacts directly with

JHEP10(2013)158

the SM through the usual Higgs portal term, while (at tree-level) the fermionic dark fields communicate with the SM indirectly, through their interactions with φ.

2.1 The model

In order to ensure stability of DM candidates we will assume that the dark sector is invariant under some global symmetry group $\mathcal{G}$ under which all the extra fields transform non-trivially, while all SM particles are $\mathcal{G}$-singlets. For simplicity we choose $\mathcal{G} = \mathbb{Z}_2 \times \mathbb{Z}_2$ and, as mentioned previously, assume that the DM sector is composed of two majorana fermions, ν_h and ν, and one real scalar φ, which under $\mathcal{G}$,

$$\nu_h \sim [-,+] \quad \nu \sim [+,-] \quad \varphi \sim [-,-] \tag{2.1}$$

We introduce the $\mathbb{Z}_2 \times \mathbb{Z}_2$ symmetry to stabilize both the DM components; models with more complicated discrete symmetries will require additional particles.

The most general, gauge- and $\mathcal{G}$-symmetric and renormalizable potential reads:

$$V(H,\varphi) = -\mu_H^2 H^\dagger H + \lambda_H (H^\dagger H)^2 + \frac{1}{2}\mu_\varphi^2 \varphi^2 + \frac{1}{4!}\lambda_\varphi \left(\varphi^2\right)^2 + \lambda_x H^\dagger H \varphi^2 \,, \tag{2.2}$$

where H is the SM SU(2) Higgs isodoublet and λ_x parametrizes the 'Higgs-portal' interaction discussed above. The Lagrangian density for the scalar sector is then given by:

$$\mathcal{L}_{\rm scal} = \frac{1}{2}\partial_\mu \varphi \partial^\mu \varphi + D_\mu H^\dagger D^\mu H - V(H,\varphi)\,. \tag{2.3}$$

As usual, we require that the potential breaks spontaneously the electroweak symmetry via non-zero vacuum expectation value of the Higgs doublet $\langle H \rangle = (0, v/\sqrt{2})$, $v = 246$ GeV. Since we also require the $\mathcal{G}$ symmetry to remain unbroken, we assume that $\mu_\varphi^2 > 0$, so $\langle \varphi \rangle = 0$. Note that $\langle \varphi \rangle = 0$ implies there is no mass-mixing between φ and H, so that the existing collider limits on the Higgs properties are not modified. After the symmetry breaking, the physical scalars have masses ${m_H}^2 = -\mu_H^2 + 3\lambda_H v^2 = 2\mu_H^2$ and $m_\varphi^2 = \mu_\varphi^2 + \lambda_x v^2$.

The part of the DM Lagrangian involving fermions reads

$$\mathcal{L} = \frac{1}{2}\overline{\nu_h}\, i\partial\!\!\!/\, \nu_h + \frac{1}{2}\overline{\nu}\, i\partial\!\!\!/\, \nu - \frac{1}{2}\nu_h^T C \nu_h M_h - \frac{1}{2}\nu^T C \nu m_\nu + g_\nu \varphi\, \overline{\nu_h}\nu. \tag{2.4}$$

Note that the interaction between the SM and DM and the DM self-interactions are generated by just two terms:

$$\mathcal{L}_{\rm int} = -\lambda_x H^\dagger H \varphi^2 + g_\nu \varphi\, \overline{\nu_h}\nu. \tag{2.5}$$

Although this model can describe a 3 component DM sector we will introduce a further simplification by assuming that $M_h > m_\nu + m_\varphi$, which allows the fast decay $\nu_h \to \varphi\nu$. In this case only ν and φ are stable and therefore can serve as realistic DM candidates. The reactions that are relevant for the evolution of DM are $\varphi\varphi \leftrightarrow {\rm SM,SM}$ and $\varphi\varphi \leftrightarrow \nu\nu$ (we will ignore the process $\nu\nu \to {\rm SM,SM}$ that occurs at one loop). We will investigate this model as a simple realization of a 2-component scalar-fermion dark sector, using it as a laboratory where the interplay of the various dark components can be studied.

JHEP10(2013)158

It is worth noticing that the dark sector has no conserved Noetherian charges, so that all the corresponding chemical potentials vanish. This can be altered in a simple way by introducing additional fermions that can serve as Dirac partners of ν_h and ν, in which case the "dark" fermion number could be conserved; we have not done so to simplify the discussion. It is also worth mentioning that the scalar singlet could be used to tame the little hierarchy problem by canceling top-quark loop induced quadratic divergences in radiative corrections to the Higgs boson mass [14, 15, 37–41].

In the following we will fix M_h at the smallest value that ensures the fast decay of ν_h, so we will effectively deal with only four parameters: $m_\varphi, m_\nu, \lambda_x$ and g_ν. Our goal is to constrain the parameters taking into account available restrictions: theoretical (vacuum stability, unitarity/perturbativity, triviality of the scalar sector) and experimental (DM relic abundance, direct detection experiments).

2.2 Theoretical constraints

In order to stabilize the vacuum we require that the scalar potential in eq. (2.2) is bounded from below. At the tree level it implies the following conditions [42]

$$\lambda_\varphi > 0\,; \quad \lambda_x > -\sqrt{\frac{\lambda_\varphi \lambda_H}{6}} = -\frac{m_h}{2v}\sqrt{\frac{\lambda_\varphi}{3}}\,, \tag{2.6}$$

where m_h denotes the Higgs mass. Amplitudes for all possible scalar-scalar scatterings will satisfy the tree-level unitarity constraints provided [43]

$$\lambda_\varphi < 8\pi, \quad |\lambda_x| < 4\pi\,. \tag{2.7}$$

Finally, it is sufficient to require $\mu_\varphi^2 > 0$ for the global $\mathcal{G}$ symmetry to remain unbroken, which leads to the very useful inequality

$$m_\varphi^2 > \lambda_x v^2\,; \tag{2.8}$$

as a consequence, light scalars ($m_\varphi \ll v$) must couple very weakly to the SM ($\lambda_x \ll 1$) whenever $\lambda_x > 0$.

We also impose the following perturbativity limits on λ_φ, λ_x and g_ν.

$$\lambda_\varphi < 4\pi, \quad |\lambda_x| < 4\pi, \quad |g_\nu| < 4\pi \tag{2.9}$$

Separating positive and negative values of λ_x, the above constraints imply that the following regions are allowed:

$$0 < \lambda_x < \min\left[\left(\frac{m_\varphi}{v}\right)^2, 4\pi\right] \tag{2.10}$$

$$-0.74 < -\frac{m_h}{2v}\sqrt{\frac{\lambda_\varphi}{3}} < \lambda_x < 0, \tag{2.11}$$

where we have adopted in eq. (2.11) the Higgs mass $m_H = 125$ GeV and the maximal value of λ_φ consistent with unitarity (2.7).

JHEP10(2013)158

3 Dark matter density and the Boltzmann equation

In the following we will focus on the minimal model specified in section 2.1. Our goal is to determine the DM relic density and test this model against the relic density constraint derived from WMAP and the available data on direct DM detection.

We start with formulating and solving the two Boltzmann equations (BEQ) that govern the cosmological evolution of our DM candidates, the DM neutrinos (ν) and scalar singlets (φ). Ignoring loop corrections the relevant reactions are $\nu\nu \leftrightarrow \varphi\varphi$ and $\varphi\varphi \leftrightarrow$ SM SM, where the last one occurs through the Higgs portal interaction $\lambda_x H^\dagger H \varphi^2$. Therefore (at tree level) for the ν to interact with the SM, they must be first converted into φ pairs through Yukawa interactions $\propto g_\nu$. The BEQs then read:

$$\begin{aligned}
\dot{n}_\varphi + 3Hn_\varphi = &-\int \frac{\zeta_\varphi d^3p}{(2\pi)^3 2E_p}\frac{\zeta_\varphi d^3p'}{(2\pi)^3 2E'_p}\frac{\zeta_{SM} d^3q}{(2\pi)^3 2E_q}\frac{\zeta_{SM} d^3q'}{(2\pi)^3 2E'_q}\delta^4 \\
&\qquad (p+p'-q-q')|M_{\varphi\varphi\to SMSM}|^2\left(\tilde{f}_\varphi\tilde{f}_\varphi - \tilde{f}^{EQ}_\varphi\tilde{f}^{EQ}_\varphi\right) \\
&-\int \frac{\zeta_\varphi d^3p}{(2\pi)^3 2E_p}\frac{\zeta_\varphi d^3p'}{(2\pi)^3 2E'_p}\frac{\zeta_\nu d^3q}{(2\pi)^3 2E_q}\frac{\zeta_\nu d^3q'}{(2\pi)^3 2E'_q}\delta^4 \\
&\qquad (p+p'-q-q')|M_{\varphi\varphi\to\nu\nu}|^2\left(\tilde{f}_\varphi\tilde{f}_\varphi - \tilde{f}_\nu\tilde{f}_\nu\right) \\
\dot{n}_\nu + 3Hn_\nu = &-\int \frac{\zeta_\varphi d^3p}{(2\pi)^3 2E_p}\frac{\zeta_\varphi d^3p'}{(2\pi)^3 2E'_p}\frac{\zeta_\nu d^3q}{(2\pi)^3 2E_q}\frac{\zeta_\nu d^3q'}{(2\pi)^3 2E'_q}\delta^4 \\
&\qquad (p+p'-q-q')|M_{\varphi\varphi\to\nu\nu}|^2\left(\tilde{f}_\nu\tilde{f}_\nu - \tilde{f}_\varphi\tilde{f}_\varphi\right)
\end{aligned} \tag{3.1}$$

where n_X denote the number density of $X = \nu, \varphi$, and n_X^{EQ} the corresponding equilibrium densities; a dot denotes a time derivative, $M_{i\to f}$ is the amplitude for the process $i \to f$ (note that $M_{\varphi\varphi\to\nu\nu} = M_{\nu\nu\to\varphi\varphi}$); $\zeta_i,\ i = \varphi,\ \nu, SM$ are the numbers of internal degrees of freedom ($\zeta_\varphi = 1$ and $\zeta_\nu = 2$, since the ν are Majorana particles), and the matrix element squared $|M|^2$ contains an average over the initial and final spins together with the corresponding $1/n!$ factors for n identical particles in the initial and final states; H denotes the Hubble parameter. The phase space density $\tilde{f}_X$ and an equilibrium density $\tilde{f}_X^{EQ}$ are related to corresponding number densities as follows:

$$n_X = \int \frac{\zeta_X d^3p}{(2\pi)^3 2E}\tilde{f}_X, \quad n_X^{EQ} = \int \frac{\zeta_X d^3p}{(2\pi)^3 2E}\tilde{f}_X^{EQ}, \quad \tilde{f}_X^{EQ} = \frac{1}{e^{E/T}\pm 1}, \quad X = \varphi, \nu \tag{3.2}$$

where, as mentioned above, the chemical potential vanishes, and $\pm$ refers to fermions and bosons, respectively. To simplify BEQs we will use the thermally averaged cross section $\langle\sigma_{XX\to YY}v\rangle$, defined as:

$$\begin{aligned}
\langle\sigma_{XX\to YY}v\rangle \equiv &\frac{1}{\left(n_X^{EQ}\right)^2}\int \frac{\zeta_X d^3p}{(2\pi)^3 2E_p}\frac{\zeta_X d^3p'}{(2\pi)^3 2E'_p}\frac{\zeta_Y d^3q}{(2\pi)^3 2E_q}\frac{\zeta_Y d^3q'}{(2\pi)^3 2E'_q}\times \\
&\delta^4(p+p'-q-q')|M_{XX\to YY}|^2 e^{-(E_p+E'_p)/T}
\end{aligned} \tag{3.3}$$

JHEP10(2013)158

Assuming kinetic equilibrium and neglecting possible effects of quantum statistics the BEQs in eq. (3.1) simplify considerably:

$$\begin{aligned}\dot{n}_\varphi + 3Hn_\varphi &= -\langle\sigma_{\varphi\varphi\to SM\,SM}v\rangle\left(n_\varphi^2 - n_\varphi^{EQ2}\right) - \left(\langle\sigma_{\varphi\varphi\to\nu\nu}v\rangle n_\varphi^2 - \langle\sigma_{\nu\nu\to\varphi\varphi}v\rangle n_\nu^2\right)\\ \dot{n}_\nu + 3Hn_\nu &= -\left(\langle\sigma_{\nu\nu\to\varphi\varphi}v\rangle n_\nu^2 - \langle\sigma_{\varphi\varphi\to\nu\nu}v\rangle n_\varphi^2\right)\end{aligned} \tag{3.4}$$

where it is important to remember that

$$\langle\sigma_{\nu\nu\to\varphi\varphi}v\rangle = \left(\frac{n_\varphi^{EQ}}{n_\nu^{EQ}}\right)^2 \langle\sigma_{\varphi\varphi\to\nu\nu}v\rangle \tag{3.5}$$

The above relation restates that there are just two independent cross sections that influence the dynamics of DM density evolution: $\langle\sigma_{\varphi\varphi\to SM\,SM}v\rangle$ and $\langle\sigma_{\varphi\varphi\to\nu\nu}v\rangle$; the first one is well known (see e.g. [14, 15]) nevertheless it is included in the appendix A for completeness. The Feynman diagram and the corresponding cross section for the process $\varphi\varphi \to \nu\nu$ are also shown in the appendix. The interactions between φ and ν involve an exchange of a virtual heavy neutrino ν_h; if the corresponding mass M_h is very large $\langle\sigma_{\varphi\varphi\to\nu\nu}v\rangle$ is strongly suppressed, which leads to an over abundance of ν. To remedy this we will assume M_h as small as allowed by the requirement of ν_h being unstable: we adopt $M_h = m_\varphi + m_\nu + \Delta M_\nu$, with fixed $\Delta M_\nu = 10$ GeV. Then the cross sections are parameterized by four parameters: m_φ, m_ν, the Yukawa coupling g_ν and the Higgs portal coupling λ_x.

3.1 Solving BEQ

Instead of a number density (n_X) it is more convenient to use the number density normalized to T^3, so in the following we adopt $f_X(T) \equiv n_X(T)/T^3$ (not to be confused with the phase-space density $\tilde{f}$ introduced previously). The initial conditions are fixed at large temperature $T_{\rm ini} = \max(m_\varphi, m_\nu)$; we assume that the couplings λ_x and g_ν are large enough so that at $T_{\rm ini}$ both DM components are in equilibrium with the SM (the SM is assumed to be in equilibrium); hence, $f_X(T_{\rm ini}) = n_X^{EQ}(T_{\rm ini})/T_{\rm ini}^3$. As the Universe cools the DM components eventually decouple from the SM when their rate of interaction becomes smaller than the rate of expansion of the universe. Since here we are looking for cold DM (CDM) candidates, we will consider only cases where this decoupling occurs when both ν an φ are non-relativistic. In the following, we will solve the BEQs (3.4) and determine the present, i.e. at $T = T_{\rm CMB} = 2.37 \cdot 10^{-13}$ GeV, DM abundance.

The solutions can be classified according to the mass hierarchy in the dark sector:

Case A: $m_\nu > m_\varphi$

Case B: $m_\nu < m_\varphi$

The dynamics of the DM number density evolution turns out to be very different for these two cases, as we will see.

If $m_\nu > m_\varphi$ (Case A), there is a temperature range where the φ do not have enough energy to create ν pairs, so the thermally averaged cross section $\langle\sigma_{\varphi\varphi\to\nu\nu}v\rangle \to 0$ below that temperature; on the other hand, neutrinos still have enough energy to maintain a high rate

JHEP10(2013)158

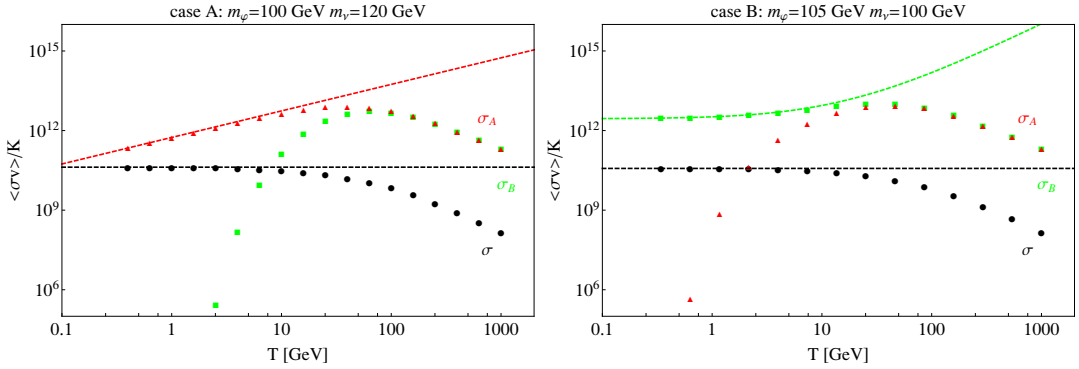

Figure 1. Thermally averaged cross sections $\sigma \equiv \langle\sigma_{\varphi\varphi\to SM\,SM}v\rangle/K$ (black points); $\sigma_B \equiv\langle\sigma_{\varphi\varphi\to\nu\nu}v\rangle/K$ (green points); $\sigma_A \equiv\langle\sigma_{\nu\nu\to\varphi\varphi}v\rangle/K$ (red points), as a functions of T (in GeV), for $\lambda_x = .1$ and $g_\nu = 2.5$. In the left panel: $m_\varphi = 100\,\text{GeV}$, $m_\nu = 120\,\text{GeV}$ (case A); in the right panel: $m_\varphi = 120\,\text{GeV}$, $m_\nu = 100\,\text{GeV}$ (case B). The factor K is defined in (3.6)

of annihilation $\nu\nu \to \varphi\varphi$. This is illustrated in the left panel of figure 1 where $\langle\sigma_{\varphi\varphi\to\nu\nu}v\rangle/K$ is seen to drop precipitously below 10 GeV while $\langle\sigma_{\varphi\varphi\to SM\,SM}v\rangle/K$ approaches a constant value already at $T \sim 5$ GeV. $\langle\sigma_{\nu\nu\to\varphi\varphi}v\rangle/K$ is vanishing at $T \to 0$ as will be discussed below. The K factor is defined as follows

$$K \equiv \sqrt{\frac{4\pi^3 g(T)}{45 m_{Pl}^2}} \tag{3.6}$$

where $g(T)$ is the number of relativistic degrees of freedom, and m_{Pl} the Planck mass. K appears in the BEQs for the normalized number densities $f_X(T) \equiv n_X(T)/T^3$. In contrast, for $m_\varphi > m_\nu$ (Case B), it is $\langle\sigma_{\nu\nu\to\varphi\varphi}v\rangle/K$ that becomes very small at small temperatures (right panel of figure 1), while $\langle\sigma_{\varphi\varphi\to SM\,SM}v\rangle/K$ and $\langle\sigma_{\varphi\varphi\to\nu\nu}v\rangle/K$ tend to a constant value, we will return to this issue in section 3.1.3.

3.1.1 Case A. ($m_\nu > m_\varphi$) - numerical solutions

In terms of the normalized number densities $f_X(T)$ defined earlier the BEQs (3.4) for case A become

$$f'_\varphi = \sigma\left[f_\varphi^2 - f_\varphi^{EQ\,2}\right] + \sigma_A\left[\left(\frac{f_\nu^{EQ}}{f_\varphi^{EQ}}\right)^2 f_\varphi^2 - f_\nu^2\right] \tag{3.7}$$

$$f'_\nu = \sigma_A\left[f_\nu^2 - \left(\frac{f_\nu^{EQ}}{f_\varphi^{EQ}}\right)^2 f_\varphi^2\right], \tag{3.8}$$

where f'_X denotes a derivative with respect to T and $\sigma \equiv \langle\sigma_{\varphi\varphi\to SM\,SM}v\rangle/K$, $\sigma_A \equiv \langle\sigma_{\nu\nu\to\varphi\varphi}v\rangle/K$; note that σ, σ_A have dimensions of mass^{-1}. Since in the non-relativistic limit σ_A is vanishing (as implied by angular momentum and parity conservation) therefore solving numerically the BEQs for the case A we have approximated σ_A by keeping only linear terms in the expansion of σ_A in powers of x_φ^{-1} where $x_\varphi \equiv m_\varphi/T$, see [44]. It was

JHEP10(2013)158

assumed that σ is T-independent. The quality of this approximation can be estimated from the left panel of figure 1. We have also verified this approximation for a number of points in the parameter space by comparing results for $f_\varphi(T_{\rm CMB})$ and $f_\nu(T_{\rm CMB})$ obtained through exact numerical solution with the one obtained adopting expansion of σ_A, relative errors obtained for the case A are: $\delta_\varphi^A \simeq 2.3\%$, $\delta_\nu^A \simeq 1.4\%$.

Examples of numerical solutions of BEQs (3.7)–(3.8) for various illustrative parameter choices are shown in figure 2. The plots on the left hand side panels correspond to case A, while case B examples are presented on the right hand side .

For case A we see that the ν (red dashed line), which are heavier, decouple from equilibrium (solid red line) before (i.e. at a higher temperature) the φ (black dashed line); after decoupling from the scalars the ν quickly freeze-out. Sometime later (at a lower temperature) the φ decouple from the SM, and since there is no communication between dark neutrinos and scalars, the latter immediately freeze-out.

It is seen from left panels of figure 2, the resulting low-temperature densities for ν and φ are similar (note the logarithmic scale), which is a signal that both components decouple form equilibrium roughly at the same x ($\sim 20-30$) as is typical for the standard cold DM scenario. Note also that for fixed m_φ, the scalar decoupling temperature T_f^φ and the scalar DM relic density are insensitive to m_ν, as a consequence of the early decoupling of the ν. Again this is an indication that both components evolve roughly independently. The dark neutrino decoupling temperature, T_f^ν grows with m_ν (since m_ν/T_f^ν is roughly constant).

The green line in figure 2 refers to solutions for scalar DM density when the fermionic DM component is absent. One can see that in case A (the left panels) the decoupling temperature of the scalar DM in the two component scenario is roughly the same as in the one component scenario with the same m_φ and λ_x, though the relic density is usually (depending on parameters chosen) smaller in the single component case.

3.1.2 Case A. ($m_\nu > m_\varphi$) - approximate analytical solutions

In the standard case of a single cold DM candidate, it is easy to find an approximate analytical solution of the BEQs that allows to determine the abundance of DM at low temperatures (see for example [45, 46]). The solution is often sufficiently accurate, so that one can avoid obtaining the numerical solutions of the BEQs. In this subsection we will derive an analogous approximate solution within our model of two-component DM for case A.

We begin by defining $\Delta_\varphi \equiv f_\varphi - f_\varphi^{EQ}$, $\Delta_\nu \equiv f_\nu - f_\nu^{EQ}$, which parameterize the deviation from equilibrium in the solutions. Then we can rewrite the BEQs (3.7)–(3.8) as:

$$\Delta'_\varphi = \sigma\Delta_\varphi\left[\Delta_\varphi + 2f_\varphi^{EQ}\right] + \sigma_A\left[\left(\frac{f_\nu^{EQ}}{f_\varphi^{EQ}}\right)^2\Delta_\varphi(\Delta_\varphi + 2f_\varphi^{EQ}) - \Delta_\nu(\Delta_\nu + 2f_\nu^{EQ})\right] - f_\varphi^{EQ\,\prime} \quad (3.9)$$

$$\Delta'_\nu = \sigma_A\left[\Delta_\nu(\Delta_\nu + 2f_\nu^{EQ}) - \left(\frac{f_\nu^{EQ}}{f_\varphi^{EQ}}\right)^2\Delta_\varphi(\Delta_\varphi + 2f_\varphi^{EQ})\right] - f_\nu^{EQ\,\prime} \quad (3.10)$$

where the primes denote temperature derivatives. Let's consider first the high temperature region - before decoupling of the DM candidates. At these temperatures f_φ, f_ν track f_φ^{EQ}, f_ν^{EQ} very closely, so that $\Delta_{\varphi,\nu}$ and $\Delta'_{\varphi,\nu}$ are very small. The corresponding solution

JHEP10(2013)158

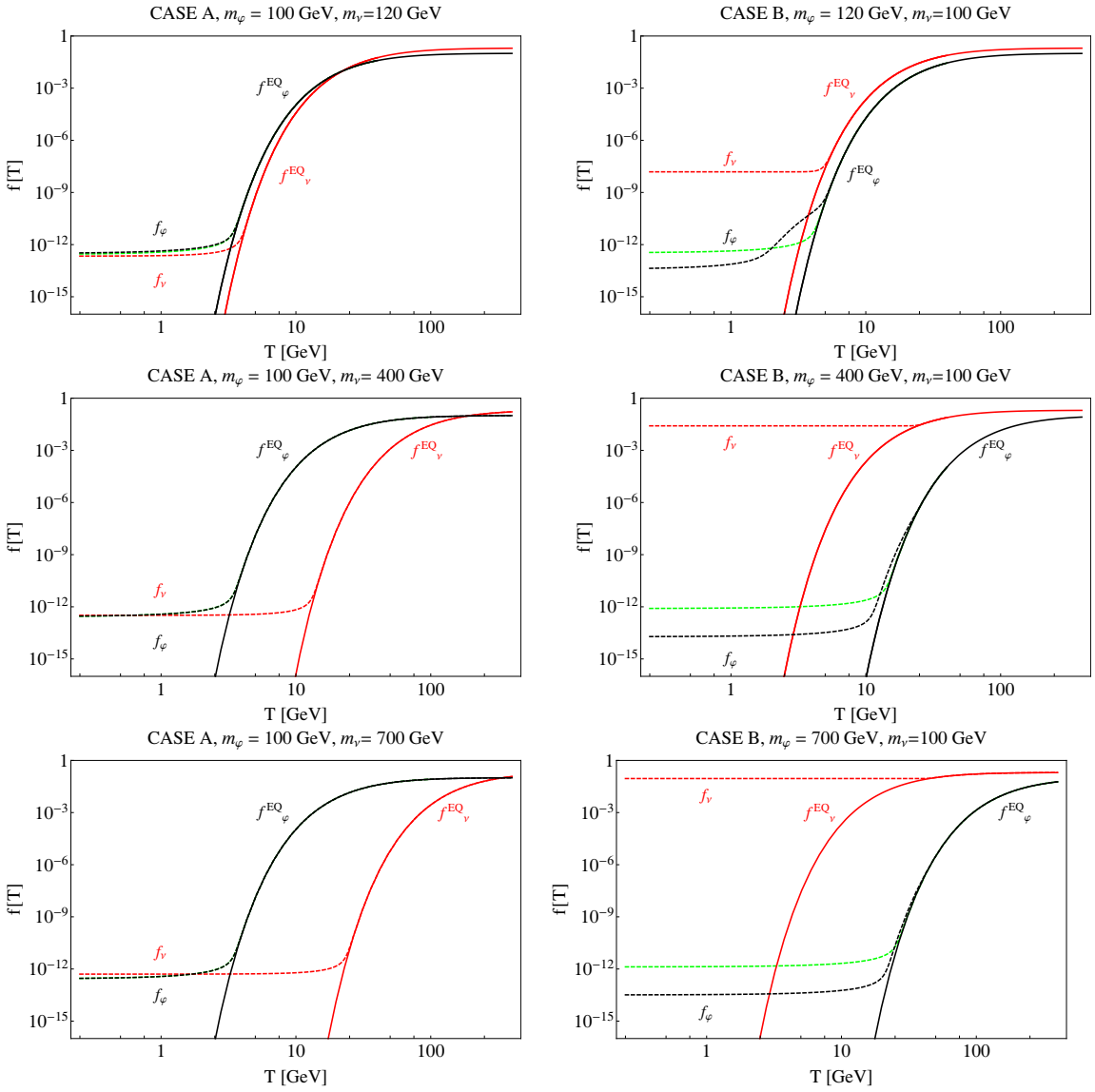

Figure 2. Solutions to the BEQs for case A (left panels) and case B (right panels) for $\lambda_x = 0.1$ and $g_\nu = 2.5$. Scalar and neutrino DM masses are specified above each panel. Solid black (red) lines correspond to the equilibrium distributions, f_φ^{EQ} (f_ν^{EQ}) for scalars (neutrinos), dashed lines are the corresponding numerical solutions of the BEQs. Green dashed lines show numerical solutions of a single BEQ for scalars without neutrinos present in the theory.

to (3.10) is obtained by neglecting $\Delta'_{\varphi,\nu}$ as well as all terms proportional to $(f_\nu^{EQ}/f_\varphi^{EQ})^2 \propto e^{-2(m_\nu - m_\varphi)/T}$ (since in this case $m_\nu > m_\varphi$):

$$\Delta_\varphi(T) \simeq \frac{1}{\sigma(\Delta_\varphi + 2f_\varphi^{EQ})}\left(f_\varphi^{EQ\prime} + f_\nu^{EQ\prime}\right) \tag{3.11}$$

$$\Delta_\nu(T) \simeq \frac{f_\nu^{EQ\prime}}{\sigma_A(\Delta_\nu + 2f_\nu^{EQ})} \tag{3.12}$$

JHEP10(2013)158

We define the decoupling temperature (freeze-out temperature)[1] for scalars (T_f^φ) and neutrinos (T_f^ν) as the temperatures at which $\Delta_\varphi(T_f^\varphi) = c_\varphi f_\varphi^{EQ}(T_f^\varphi)$ and $\Delta_\nu(T_f^\nu) = c_\nu f_\nu^{EQ}(T_f^\nu)$ with $c_{\varphi,\nu} = O(1)$. This means that at decoupling temperature the number density differs from the corresponding equilibrium density roughly by a factor of few. We will later assume $c_\varphi(c_\varphi + 2) = c_\nu(c_\nu + 2) = 1$, because this choice of c_φ, c_ν will provide good agreement with numerical solutions and simplifies the analytical expressions. The freeze-out temperatures T_f^φ and $T_f^\nu$are then determined by

$$f_\varphi^{EQ}(T_f^\varphi) \simeq \frac{1}{c_\varphi(2+c_\varphi)\sigma}\left[\frac{m_\varphi}{T_f^{\varphi 2}} + \frac{f_\nu^{EQ}(T_f^\varphi)}{f_\varphi^{EQ}(T_f^\varphi)}\frac{m_\nu}{T_f^{\varphi 2}}\right] \simeq \frac{m_\varphi}{\sigma T_f^{\varphi 2}} \tag{3.13}$$

$$f_\nu^{EQ}(T_f^\nu) \simeq \frac{m_\nu}{\sigma_A(T_f^\nu)T_f^{\nu 2}} \tag{3.14}$$

where we have substituted out choice $c_{\nu,\varphi} = \sqrt{2} - 1$. In obtaining this we have assumed, consistent with the cold dark matter requirement, that the parameters are such that $m_\nu, m_\varphi \gtrsim T_f^{\nu,\varphi}$, and kept only the leading terms. Once the freeze-out temperatures $T_f^{\varphi,\nu}$ are obtained by solving (3.13)–(3.14), $\Delta_\varphi(T_f^\varphi)$ and $\Delta_\nu(T_f^\nu)$ can be calculated using eqs. (3.11)–(3.12). It turns out that for the choice $c_{\nu,\varphi} = \sqrt{2}-1$ our approximate equations for $T_f^{\nu,\varphi}$ reproduce the exact ones (found numerically) very well, typical errors calculated from 20 random points are 0.9% for T_f^ν and 1.2% for T_f^φ.

After freeze-out the number densities remain much larger than their equilibrium counterparts, so that $\Delta_{\nu,\varphi} \simeq f_{\nu,\varphi}$ and we can neglect all terms containing $f_{\varphi,\nu}^{EQ}$ and $f_{\varphi,\nu}^{EQ\prime}$ as well as all terms proportional to $(f_\nu^{EQ}/f_\varphi^{EQ})^2 \propto e^{-2(m_\nu - m_\varphi)/T}$ In this case (3.10) simplifies to $\Delta_\nu' = \sigma_A\Delta_\nu^2$ with solutions

$$\Delta_\nu(T) = \frac{\Delta_\nu(T_f^\nu)}{1 - \Delta_\nu(T_f^\nu)\int_{T_f^\nu}^T \sigma_A(T')dT'} \quad \Rightarrow \quad \Delta_\nu(T_{\rm CMB}) \simeq \frac{\Delta_\nu(T_f^\nu)}{1 + \sigma_A(T_f^\nu)T_f^\nu\Delta_\nu(T_f^\nu)/2} \tag{3.15}$$

where in this we assumed $\sigma_A \propto T$, as discussed above and illustrated in figure 1. Using now (3.14) we find that $\sigma_A(T_f^\nu)T_f^\nu\Delta_\nu(T_f^\nu) > 1$ so we obtain

$$f_\nu(T_{CMB}) \simeq \Delta_\nu(T_{\rm CMB}) \simeq \frac{2}{\sigma_A(T_f^\nu)T_f^\nu} \tag{3.16}$$

After freeze-out the evolution equation for φ becomes

$$\Delta_\varphi' \simeq \sigma\Delta_\varphi^2 - \sigma_A\Delta_\nu^2 \tag{3.17}$$

with initial condition $\Delta_\varphi(T_f^\varphi) \simeq c_\varphi m_\varphi/(\sigma {T_f^\varphi}^2)$ derived from (3.13). In solving this equation we will approximate Δ_ν by its value at $T_{\rm CMB}$ and σ_A by its value at T_f^ν (we have verified the accuracy of these assumptions by comparing the analytic results with the exact numerical

[1] In the case A, the freeze-out happens immediately after decoupling, therefore the decoupling temperature and the freeze-out temperature are identical. As we will show shortly, this is not true in the case B.

JHEP10(2013)158

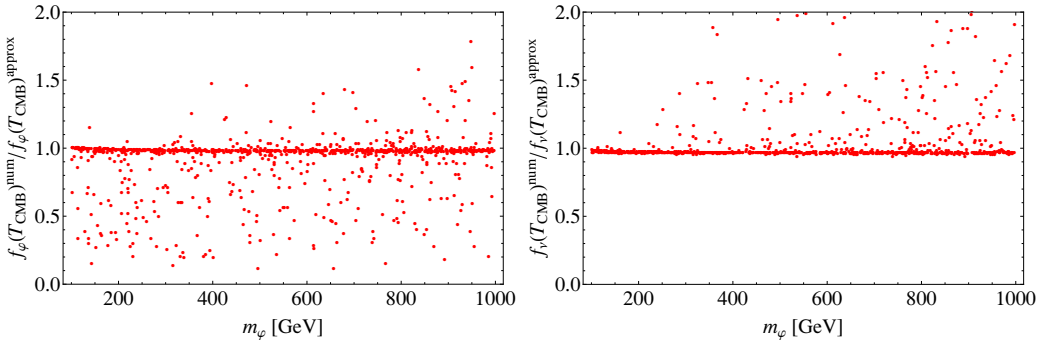

Figure 3. The ratio $f_X(T_{\rm CMB})^{\rm num}/f_X(T_{\rm CMB})^{\rm approx}$ for case A for scalars (left panel) and neutrinos (right panel) as a function of scalar DM mass. 500 parameter points $(m_\varphi, m_\nu, \lambda_x, g_\nu)$ were chosen randomly within the ranges 10 GeV $< m_\varphi, m_\nu <$ 1 TeV, $0.001 < \lambda_x < 4\pi$ and $0.1 < g_\nu < 4\pi$.

results in a set of randomly selected paramter points). Using these approximations the solution is easy to find:

$$\Delta_\varphi(T) = \frac{r_f}{\sigma T_f^\varphi}\frac{u+\tanh[r_f(1-T/T_f^\varphi)]}{1+u\tanh[r_f(1-T/T_f^\varphi)]}; \quad r_f = 2\,\frac{T_f^\varphi}{T_f^\nu}\sqrt{\frac{\sigma}{\sigma_A(T_f^\varphi)}},\ u = \frac{c_\varphi m_\varphi}{r_f T_f^\varphi} \tag{3.18}$$

Note that

$$r_f \propto 2\frac{m_\varphi}{m_\nu}\sqrt{\frac{\sigma}{\sigma_A(T_f^\nu)}} \tag{3.19}$$

therefore in the case A, its value is typically small. Expanding (3.18) around $r_f = 0$ one obtains in the leading order

$$f_\varphi(T) \simeq \Delta_\varphi(T) \simeq \Delta_\varphi(T_{\rm CMB}) \simeq \frac{1}{\sigma T_f^\varphi}\,, \tag{3.20}$$

The above expression shows that the resulting low-temperature φ density is roughly the same as it would be in the case without neutrinos at all. That is also seen in the left panels of figure 2 where dashed green lines (no neutrinos) coincides with black ones (the full system). Since x_f for ν and φ are similar therefore so are the densities.

The accuracy of the above results can be gauged by calculating the ratio of $f_X^{\rm num}$, the numerical solution, over the corresponding analytical approximate solution, $f_X^{\rm approx}$, at $T = T_{\rm CMB}$, the present Universe temperature; the results are presented in figure 3. As one can see, the approximations are often satisfactory for the chosen parameter space. In general, the result for $f_\nu^{\rm approx}$ are more reliable and become more accurate as the splitting between the φ and ν masses increases (which is natural as we are neglecting terms containing $(f_\nu^{EQ}/f_\varphi^{EQ})^2 \propto e^{-2(m_\nu - m_\varphi)/T}$). The quality of the approximation seems to be independent of λ_x, both for f_φ and f_ν.

3.1.3 Case B. ($m_\nu < m_\varphi$)

When $m_\varphi > m_\nu$ we again assume equilibrium at high temperatures. As the temperature drops, DM particles become non-relativistic and the neutrinos will no longer have

JHEP10(2013)158

enough energy to create pairs of the heavier scalars through annihilation $\nu\nu \to \varphi\varphi$, so that $\langle\sigma_{\nu\nu\to\varphi\varphi}v\rangle \to 0$ as $T \to 0$. On the other hand the rate of ν-pair creation, $\varphi\varphi \to \nu\nu$ has a non-zero limit as $T \to 0$ (see the right panel of figure 1).

In this case the BEQs (3.4) read

$$f'_\varphi = \sigma\left[f_\varphi^2 - f_\varphi^{EQ2}\right] + \sigma_B\left[f_\varphi^2 - \left(\frac{f_\varphi^{EQ}}{f_\nu^{EQ}}\right)^2 f_\nu^2\right] \tag{3.21}$$

$$f'_\nu = \sigma_B\left[\left(\frac{f_\varphi^{EQ}}{f_\nu^{EQ}}\right)^2 f_\nu^2 - f_\varphi^2\right] \tag{3.22}$$

where $\sigma_B \equiv \langle\sigma_{\varphi\varphi\to\nu\nu}v\rangle/K$. As it is shown in the right panel of figure 1, for low temperatures σ is well approximated by a constant while for σ_B we used low-temperature expansion keeping linear and quadratic terms in x^{-1}. We have estimated the quality of the approximation by comparing the exact numerical integration of the BEQ's for a number of points in the parameter space with the one obtained with quadratic expansion of σ_B, resulting errors for $f_\varphi(T_{\rm CMB})$ and $f_\nu(T_{\rm CMB})$ are the following $\delta_\varphi^B = 6.3\%$, $\delta_\nu^B = 2.6\%$. It is also useful to notice that the ratio of equilibrium distributions, $\left(f_\varphi^{EQ}/f_\nu^{EQ}\right)^2 \propto e^{-2(m_\varphi - m_\nu)/T}$ vanishes as $T \to 0$ since $m_\nu < m_\varphi$.

Numerical solutions of (3.21), (3.22) are shown in the right panel of figure 2, where the neutrino mass was fixed at $m_\nu = 100$ GeV for three choices of scalar mass: $m_\varphi = 120, 400$ and 700 GeV. Note that for parameters adopted in the figure ($\lambda_x = 0.1$, $g_\nu = 2.5$), ν and φ decouple roughly simultaneously; we have verified numerically that this is typical throughout most of the relevant region of parameter space.[2] Since $T_f^\nu \simeq T_f^\varphi$ and $f_\varphi^{EQ} < f_\nu^{EQ}$ for $m_\nu < m_\varphi$, the asymptotic low-temperature density will be larger for neutrinos, $f_\varphi(T) < f_\nu(T)$. Therefore, in case B, it is typical that the number density of DM at low temperatures is dominated by neutrinos. In fact, f_ν domination at low temperatures can be understood intuitively since neutrinos do no couple directly to the SM, and in consequence, they annihilate into SM particles slower than scalars.

Contrary to naive expectation, it is remarkable that in case B and for fixed m_ν the fermion freeze-out temperature is strongly dependent on m_φ (right panel of figure 2), it varies from $T_f^\nu \simeq 4$ GeV for $m_\varphi = 120$ GeV to $T_f^\nu \simeq 30$ GeV for $m_\varphi = 700$ GeV. Note that in this case x_f differs from its standard value $20 - 30$, for instance for $m_\varphi = 700$ GeV and $m_\nu = 100$ GeV corresponding values are $x_\varphi^f \simeq 23$ and $x_\nu^f \simeq 3$ for φ and ν respectively. This results in a rapid grow of low-temperature f_ν with m_φ at fixed m_ν: $f_\nu(T_{\rm CMB}) \sim 10^{-8}$ at $m_\varphi = 120$ GeV, to $f_\nu(T_{\rm CMB}) \sim 10^{-1}$ at $m_\varphi = 700$ GeV. On the other hand, the low-temperature $f_\varphi(T_{\rm CMB})$ is roughly independent of m_φ, even though the scalar decoupling temperature, T_f^φ varies with m_φ. This case nicely illustrates the dramatic influence of the presence and interaction among DM components upon their thermal evolution.

[2] Neutrinos decouple earlier for small neutrino Yukawa coupling $g_\nu \sim 0.1$, but in this case the DM relic abundance does not match the one derived from the WMAP data, which requires larger Yukawa couplings $g_\nu \gtrsim 1.8$.

JHEP10(2013)158

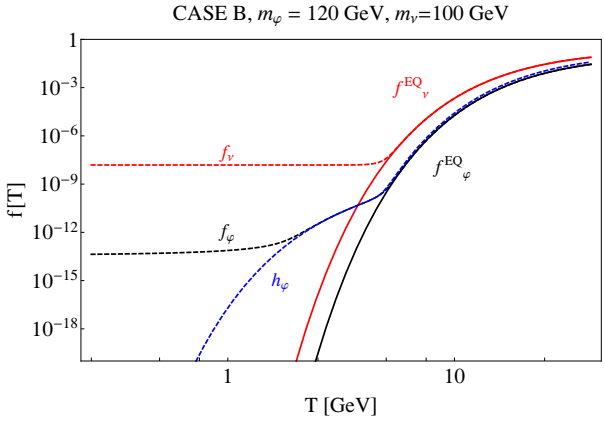

Figure 4. Solution of the BEQs, case B ($m_\varphi = 120\,\text{GeV}$, $m_\nu = 100\,\text{GeV}$); for $\lambda_x = 0.1$, $g_\nu = 2.5$. Solid black (red) line illustrates equilibrium distributions, f_φ^{EQ} (f_ν^{EQ}) for scalars (neutrinos), dashed lines are the corresponding numerical solutions of the BEQs. Blue dashed line shows the distribution h_φ from (3.23).

Another comment is in order here. As one can clearly see in first panel on the right of figure 2, there are parameter ranges such that after decoupling from equilibrium, scalars (black dashed line) do not freeze-out immediately (in contrast to single-component DM or in case A): f_φ deviates from equilibrium, but is still temperature dependent and only later freezes out. This happens because even below the temperature at which the ν and φ decouple from the equilibrium with the SM, φ pairs can still annihilate into ν pairs. This effect can be seen from the BEQs (3.21)–(3.22). After the ν decouple, we have $f_\nu \gg f_\nu^{EQ}$ and the BEQ for scalars, eq. (3.21) becomes

$$f'_\varphi = (\sigma + \sigma_B)\left(f_\varphi^2 - h_\varphi^2\right)\,, \quad h_\varphi^2 = f_\varphi^{EQ\,2}\left[\frac{\sigma}{\sigma+\sigma_B} + \left(\frac{f_\nu}{f_\nu^{EQ}}\right)^2 \frac{\sigma_B}{\sigma+\sigma_B}\right] \tag{3.23}$$

We interpret this as follows: after neutrinos decouple, scalars approach a modified "equilibrium" distribution h_φ shown as the blue dashed curve in figure 4. As it is seen in the right panels of figure 2 and in figure 4, as T decreases, f_φ will eventually decouple also from h_φ and freeze-out. In order to illustrate the difference between the modified evolution of scalars after the decoupling from f_φ^{EQ} we plot in the right panels of figure 2 also the numerical solutions of a single BEQ for scalars without neutrinos present in the theory (green dashed lines). This behavior of f_φ between decoupling and freeze-out is only possible in multi-component and self interacting DM scenarios and, to the best of our knowledge, has not been previously discussed in the literature.

The disappearance of scalars into neutrinos is, of course, more efficient and faster as the mass difference between φ and ν grows, this can also be observed in the right panels of figure 2. It is also seen that a large mass splittings results in very large neutrino low-temperature density, while scalar density remains very small, $f_\varphi \sim 10^{-12} - 10^{-13}$. It follows that upper limits on the total DM density (implied e.g. by the WMAP data) favor small mass splitting.

JHEP10(2013)158

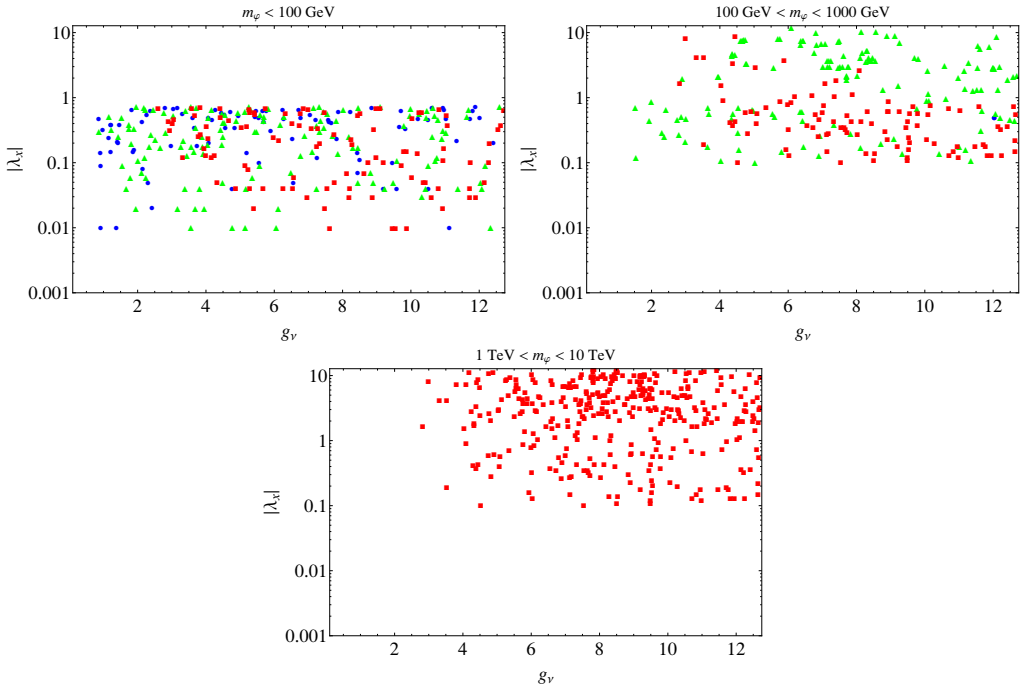

Figure 5. Points (obtained by solving the BEQs numerically) that satisfy WMAP bound for cases A and B and projected into the (λ_x, g_ν) plane. Blue (circles): $m_\nu < 100$ GeV, green (triangles): 100 GeV $< m_\nu <$ 1 TeV red (squares): 1 TeV $< m_\nu <$ 2 TeV and for scalar DM mass ranges as indicated in each panel.

Following a strategy analogous to the one we used in case A one can also find an approximate analytical solution of the BEQs in case B. Unfortunately the accuracy of the approximation is much worse in this case, because of the difficulties in including the intermediate state where the scalars have decoupled but have not yet frozen-out. For this reason in case B we will use only numerical solutions.

4 Relic abundance

The total relic abundance of DM in our model is given by the sum of the neutrino and scalar abundances:

$$\Omega_{\rm tot} = \Omega_\nu + \Omega_\varphi = \frac{m_\nu f_\nu + m_\varphi f_\varphi}{\rho_{crit}} T_\gamma^3 \tag{4.1}$$

The experimental data on the relic density measured at the 1σ level by WMAP [8] shown in equation (1.1). In order to determine parameters of our model that satisfy the limit, we have performed a random scan over the 4-dimensional parameter space of our model $(m_\varphi, m_\nu, \lambda_x, g_\nu)$ in a range: 1 GeV $< m_\varphi <$ 10 TeV, 1 GeV $< m_\nu <$ 2 TeV, $0.001 < \lambda_x < 4\pi$ and $0.1 < g_\nu < 4\pi$. The results of the scan — points satisfying the relic abundance constraint (within 3σ) in the (λ_x, g_ν) plane, are shown in figure 5.

It is seen from figure 5 that we did not find any points satisfying the WMAP bound for $g_\nu < 0.92$. In fact, it is easy to understand why g_ν can not be very small: as is seen

JHEP10(2013)158

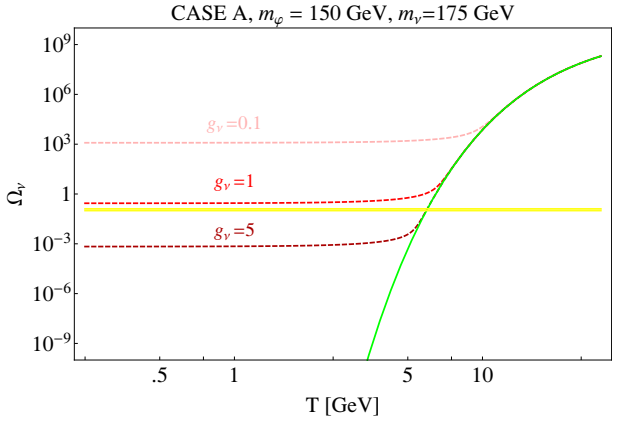

Figure 6. Solutions of the BEQs for $m_\varphi = 150\,\text{GeV}$, $m_\nu = 175\,\text{GeV}$ (case A), $\lambda_x = 1$. Pink, red, dark red lines: solutions for the neutrino abundance for $g_\nu = 0.1, 1, 5$, respectively. Yellow lines: WMAP 6σ limit on DM abundance. Green: equilibrium distribution for neutrinos at 175 GeV.

from figure 6 the relic abundance of ν increases rapidly as g_ν drops, since this suppresses annihilation into scalar pairs; g_ν must be large enough in order to avoid overabundance of neutrinos. This reasoning is supported, in the case A, by our approximate analytical solution (3.16) for which $f_\nu(T_{\rm CMB}) \propto \sigma_A^{-1} \sim g_\nu^{-4}$, so that an order of magnitude change in g_ν implies 4 orders of magnitude change in the abundance of neutrinos! From figure 5 we also observe that the WMAP constraint requires that a growing m_φ be correlated with large $|\lambda_x|$ and g_ν, so that with increasing m_φ our points are more and more concentrated in the upper right corner of the $g_\nu - \lambda_x$ plane. Note that in the lower panel only red squares survive, this is because for heavier scalar DM masses, only slightly heavier or degenerate neutrino DM masses, accompanied by large values of $|\lambda_x|$ and g_ν survive the relic density constraint. This is also easy to understand: with increasing scalar DM mass, scalar relic density increases for case A and neutrino DM density increases for both case A and case B. So, to bring the number density down within the observed limit, we need large couplings to increase the annihilation rates and, in addition, the mass splitting has to be small in order to tame the neutrino DM density; see, for example, figure 2. This is also understood from figures 7 and 8 as discussed below.

It is instructive to look into various projections of the scan points shown in figure 7. The left panels are for $\lambda_x > 0$, so the limits (2.10) are imposed, while the right ones are for $\lambda_x < 0$ in which case only the limit (2.11) applies. In each case we show, as a function of m_φ, all the remaining parameters, λ_x, g_ν and m_ν for which the WMAP bound is satisfied. The plots in figure 7 differentiate between case A (green circles) and B (dark green squares) of which the former are much more plentiful Note that the $m_\varphi - m_\nu$ projections (lower panels) show that in case B the WMAP restriction can be satisfied only for $m_\varphi \simeq m_\nu$, as dark green squares are located just below the diagonal line. In figure 8 we illustrate the effects of the m_φ-m_ν splitting on the neutrino abundance Ω_ν for case B; we can see that the WMAP bound can be met only when the masses are close enough. This can be understood from the right panels of figure 2 from which it is clear that in order to reduce f_ν, the dominant low-

JHEP10(2013)158

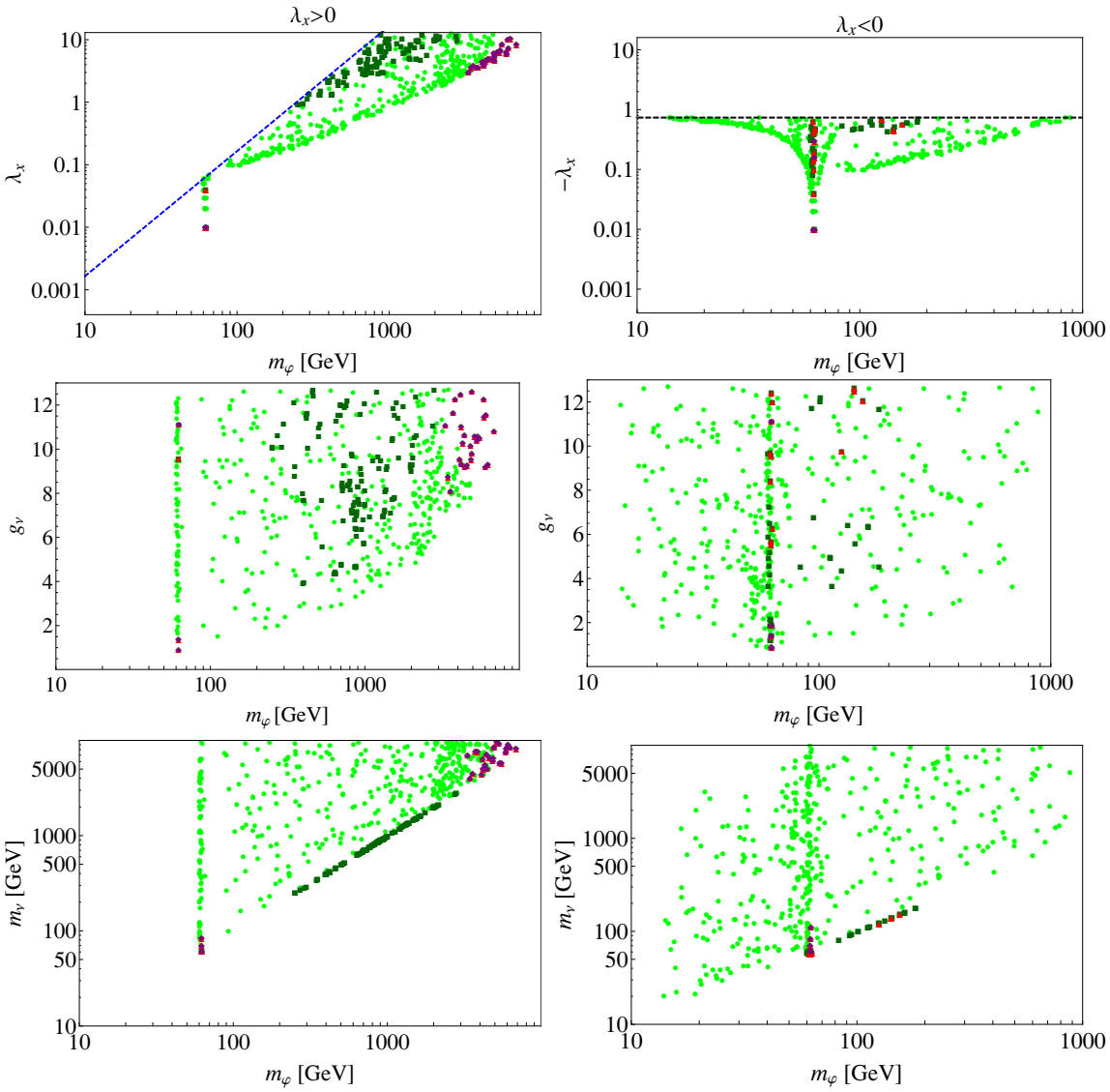

Figure 7. Points that satisfy WMAP bound within 3σ range projected into (λ_x, m_φ) (upper), (g_ν, m_φ) (middle) and (m_ν, m_φ) (lower) planes. Green circles - case A points, dark green squares - case B points. Red triangles and purple diamonds - points for which the XENON100 limit is separately satisfied, respectively by φ and ν. The consistency limit on λ_x (2.10) and the stability limit (2.11) for $\lambda_\varphi = 8\pi$ are satisfied.

JHEP10(2013)158

temperature component of DM, the splitting between m_φ and m_ν must be small; for large splittings the DM decouples and freezes-out early ($T_f^\nu \sim O(10)$ GeV), and the neutrinos do not have enough time to disappear into SM particles, leading to an unacceptably large DM relic abundance. When the mass splitting is small the neutrino annihilation into scalars (followed by scalar annihilation into SM particles) is still sufficiently efficient to yield an acceptable relic abundance. Summarizing, in case B the WMAP bound can be met only if *i)* the neutrinos freeze-out relatively late, and *ii)* $m_\nu \simeq m_\varphi$.

We also include in figure 7 points that satisfy direct detection limits from XENON100 (red triangles) and CREST-II (blue diamonds) (direct detection of DM will be discussed in detail in section 5). It is important to note already at this point that there exist three regions of φ mass which are consistent with XENON100: $m_\varphi \simeq m_h/2$, $m_\varphi \simeq 130-140$ GeV and heavy mass region $m_\varphi \gtrsim 3$ TeV.

It is also worth discussing more quantitatively the degeneracy $m_\nu \simeq m_\varphi$ required for the case B. As it is seen in the upper and middle panels of figure 2, if the mass splitting $\Delta m = m_\varphi - m_\nu$ is not too large, then the decoupling from equilibrium occurs in a range of temperatures where the "distance" between distributions, $\Delta f(T) \equiv [\log_{10} f_\varphi^{EQ}(T) - \log_{10} f_\nu^{EQ}(T)]$, is approximately T-independent, and depends mainly on Δm. Changing the coupling constants alters the decoupling temperature of both DM particles, but $\Delta f(T)$ remains unaltered. Since scalars and neutrinos decouple roughly simultaneously $\Delta f(T_{\rm CMB})$ is also a function of Δm only. It follows that, if $m_\varphi \simeq m_\nu$, the difference between the φ and ν contributions to Ω_{DM}, $\Delta\Omega = (\log_{10}\Omega_\varphi - \log_{10}\Omega_\nu)$, is roughly a function of Δm only. The minimal abundance found within the numerical scans is $\Omega \sim 10^{-8}$. In order to reach the WMAP range of abundance ($\Omega \sim 0.1$), the maximal value of $\Delta\Omega$ should be ~ 7. From figure 8 we can estimate that this value of $\Delta\Omega$ corresponds to $\Delta m \lesssim 40\,$GeV. This very rough estimate agrees with our numerical scans where we find that (in case B) the maximal allowed splitting found is $\Delta m_{\rm NUM}^{\rm MAX} = 29.8\,$GeV.

The top panel of figure 7 clearly shows the resonance region $m_\varphi \simeq m_h/2 \sim 62.5$ GeV in the (λ_x, m_φ) plane; λ_x must be small otherwise the resonant graph with a Higgs boson in the s-channel yields too large annihilation rate and consequently too small φ abundance. The intermediate mass consistent with XENON100, $m_\varphi \simeq 130 - 140$ GeV requires $\lambda_x < 0$ that causes a destructive interference between diagrams contributing to the annihilation rate so that the annihilation rate could be suppressed even with substantial λ_x. The high scalar mass region consistent with XENON100 requires large λ_x. In the middle panel of figure 7 we again observe that usually large values of g_ν are allowed by the WMAP data. In figure 9 we present allowed region in the (λ_x, m_φ) plane for both $\Omega_\varphi > \Omega_\nu$ and $\Omega_\varphi < \Omega_\nu$; it is worth noting that points that are close to the lower edge of the WMAP allowed region generally correspond to $\Omega_\varphi > \Omega_\nu$ (dark orange squares). When Ω_φ dominates φ annihilation rate must be sufficiently suppressed in order to keep the φ abundance at the WMAP level. The edge corresponds to the result for $\lambda_x = \lambda_x(m_\varphi)$ obtained for one singlet DM case investigated in [14, 15], (see figure 7 in that reference).

Figure 10 illustrates the manner in which the DM abundance is split between φ and ν.

JHEP10(2013)158

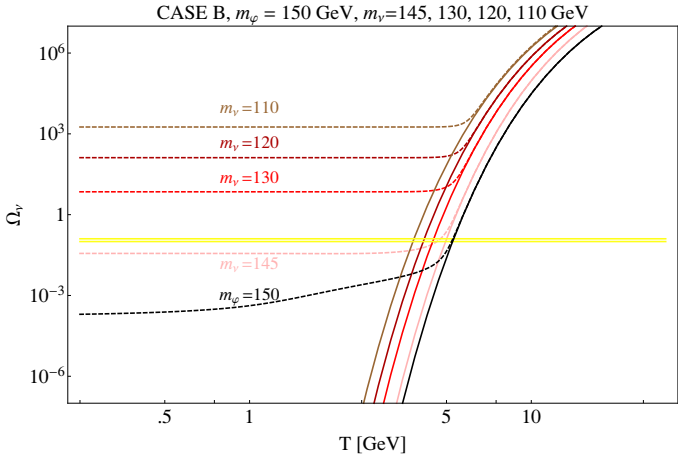

Figure 8. Solutions to the BEQs: f_φ (dashed black line), f_φ^{EQ} (solid black line) and f_ν for $m_\nu = 145, 130, 120, 110$ GeV (light red, red, dark red and brown dashed lines, respectively). In all cases we chose $m_\varphi = 150$ GeV, $\lambda_x = 1$, $g_\nu = 7.5$. Yellow lines are from the WMAP 6σ allowed region of DM abundance.

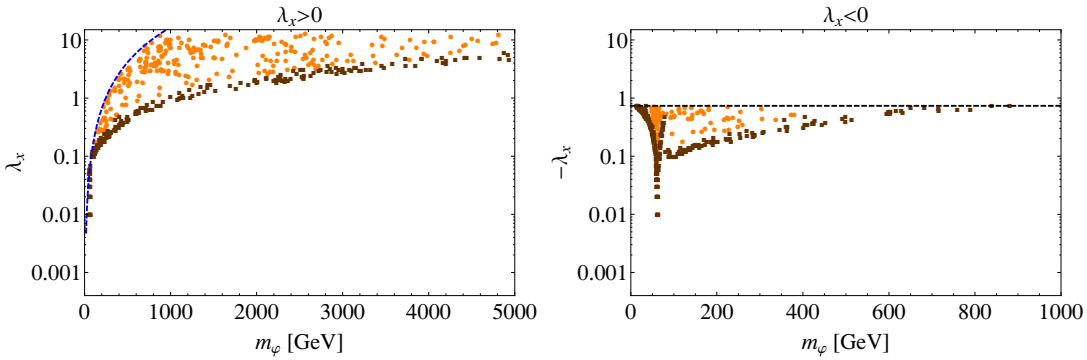

Figure 9. Points that satisfy WMAP bound within 3σ range projected into (λ_x, m_φ) plane. Orange circles - points where $\Omega_\varphi < \Omega_\nu$, dark orange squares - points where $\Omega_\varphi > \Omega_\nu$. The left panel corresponds to the solutions for positive λ_x, while the right panel is for negative λ_x. Blue dashed line is the consistency limit on λ_x (2.10), while the black horizontal dashed line is the stability limit $\lambda_\varphi = 8\pi$.

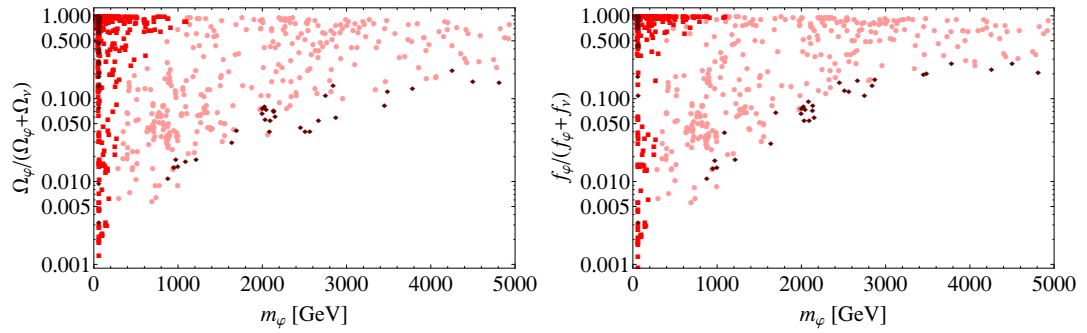

Figure 10. Relative abundance of φ (left panel) and relative number density of φ (right panel) as a function of m_φ for points that satisfy WMAP bound within 6σ. Light red points: $1 < \lambda_x < 10$; red points: $0.1 < \lambda_x < 1$; dark red points: $\lambda_x < 0.1$

JHEP10(2013)158

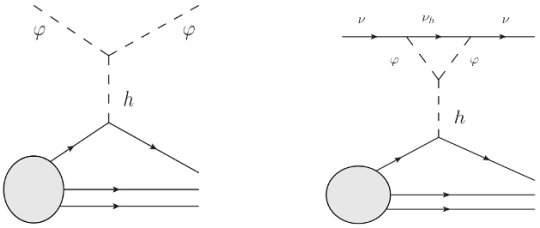

Figure 11. The Feynman diagram for the elastic scattering of DM (φ and ν) off a nucleon.

5 Direct detection

In this section we discuss constraints imposed on the model by searches for direct signals of DM particles scattering off a nuclei. We focus here on constraints obtained by the XENON100 experiment [47] as they impose strongest limits on DM - nucleon scattering cross-section $\sigma_{\mathrm{DM-N}}$ in the mass range of our interest. We will also comment on results obtained by the CREST-II experiment [48].

In our model, at the tree level, scattering of DM off nuclei originates from the interaction with the scalar DM component. Neutrino's leading contribution to the scattering appears at the one-loop level. However, as it has been multiply illustrated, the DM is often dominated by dark neutrinos. Therefore, even though ν nucleon scattering is loop induced, it might be relevant. Therefore, the dominant contributions to the scattering of DM are described by the two Feynman diagrams in figure 11. We start with φ nucleon scattering, the corresponding cross section is the following

$$\sigma_{\varphi N} = \frac{4\mu^2}{\pi}\left(\frac{\lambda_x m_N}{2m_\varphi m_h^2}\sum_q f_q^N\right)^2 \tag{5.1}$$

where the sum runs over all quark flavors q, m_n is the nucleon mass and f_q^N are the nucleon form factors as defined in [53] and $\mu \equiv m_\varphi m_N/(m_\varphi + m_N)$.

To compare the prediction for the direct detection cross section obtained within our 2-component DM scenario with experimental results from the XENON collaboration one has to take into account that the standard limits on DM direct detection assume all DM particles to be interacting with SM with the same rate. In our case, this is not true as we have two components of DM and their number densities are in general different. Therefore, to compare with the data, we need to rescale the φN cross section by a factor that accounts for the fact that two DM components are present:

$$\sigma^{\varphi}_{\mathrm{DM-N}} = \frac{n_\varphi}{n_\varphi + n_\nu}\sigma_{\varphi N}. \tag{5.2}$$

In figure 12 we plot the rescaled cross section $\sigma^{\varphi}_{\mathrm{DM-N}}$ as a function of m_φ calculated for points satisfying the WMAP bounds for cases A and B. It follows from this figure that in the resonance region $m_\varphi \simeq m_h/2$ and in the middle mass region $m_\varphi \simeq 130 - 140$ GeV direct detection constraints favor $m_\nu < m_\varphi$ (case B). However for the heavy scalars solution $m_\varphi \gtrsim 3$ TeV it turns out that $m_\nu > m_\varphi$ (case A) is required. The right panel of figure 12

JHEP10(2013)158

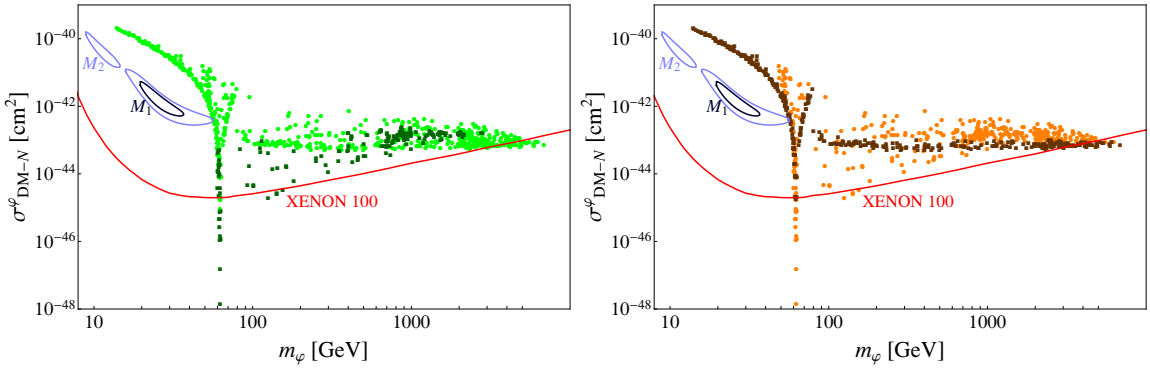

Figure 12. Plot of the cross section $\sigma^{\varphi}_{\mathrm{DM-N}}$ as a function of m_φ for points satisfying the WMAP data within 3σ; the other parameters are randomly chosen in the ranges defined in the text (including both signs of λ_x). Left panel: green circles (dark green squares) correspond to case A (case B) solutions. Right panel: orange circles (dark orange squares) correspond to $\Omega_\varphi < \Omega_\nu$ ($\Omega_\varphi > \Omega_\nu$). The red line shows the XENON100 data, and the two islands in blue indicate 1 and 2σ CRESST-II results.

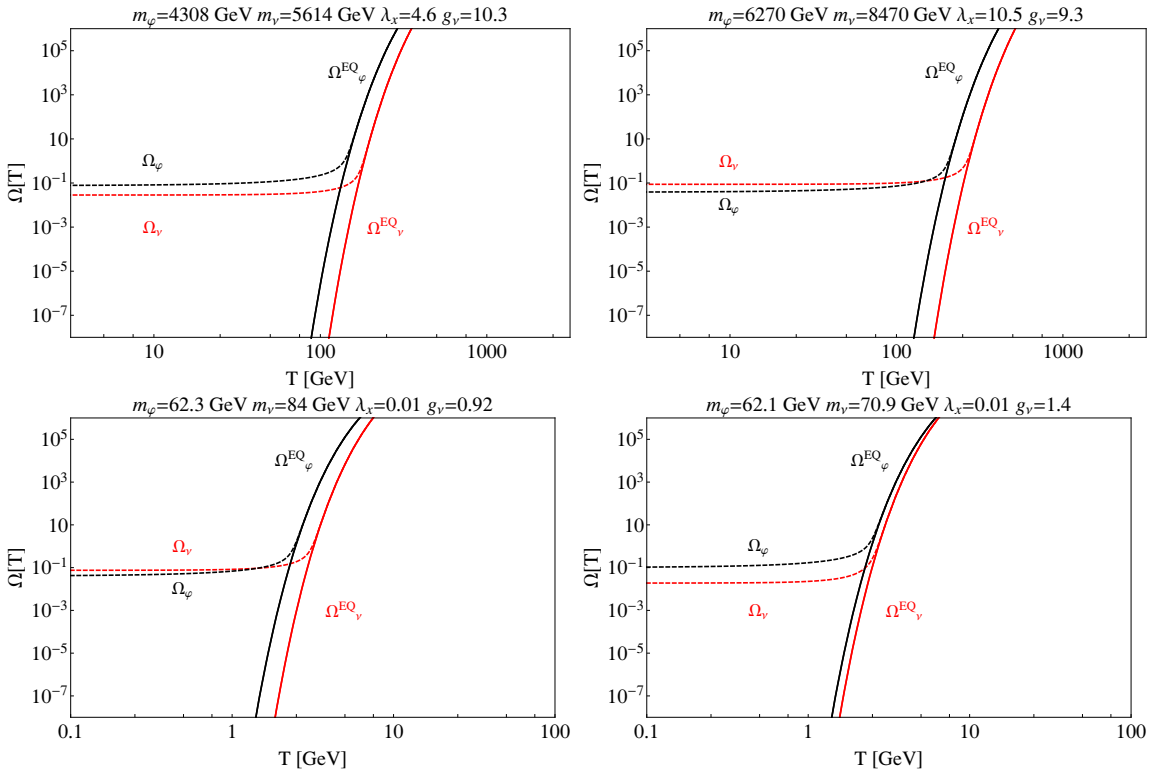

Figure 13. Selected solutions of the Boltzmann equation for parameters that satisfy both WMAP and XENON constraints.

JHEP10(2013)158

illustrates the correlation between $\sigma^{\varphi}_{\mathrm{DM-N}}$ and the relative abundance of φ and ν. We observe that in the resonance region and in middle mass region $\Omega_\varphi < \Omega_\nu$ (more neutrinos) while for the large mass $\Omega_\varphi > \Omega_\nu$ (more scalars).

As seen from figure 12 the majority of points lie above (i.e. are excluded by) the XENON100 lower limit. This is easy to understand. Using (5.1) and (5.2) we find that

$$\sigma^{\varphi}_{\mathrm{DM-N}} \propto \frac{\lambda_x^2}{m_\varphi^2} \frac{f_\varphi(T_{\mathrm{CMB}})}{f_\varphi(T_{\mathrm{CMB}}) + f_\nu(T_{\mathrm{CMB}})}. \tag{5.3}$$

In order to minimize $\sigma^{\varphi}_{\mathrm{DM-N}}$ one should (for a given m_φ) choose λ_x and $f_\varphi(T_{\mathrm{CMB}})/(f_\varphi(T_{\mathrm{CMB}}) + f_\nu(T_{\mathrm{CMB}}))$ as small as possible. These factors, however, are correlated. For a conservative estimate of the m_φ dependence we choose the lower edge of the allowed (λ_x, m_φ) region from the upper panel of figure 7, and the lower edge of the $f_\varphi(T_{\mathrm{CMB}})/(f_\varphi(T_{\mathrm{CMB}}) + f_\nu(T_{\mathrm{CMB}}))$ region found in figure 10. From figure 7 we find that for 100 GeV $< m_\varphi <$ 1000 GeV

$$\log_{10}(\lambda_{x\,\mathrm{min}}) \simeq \log_{10}\left(\frac{m_\varphi}{1\ \mathrm{GeV}}\right) - 3\,, \tag{5.4}$$

while from figure 10 we obtain

$$\log_{10}\left[\frac{f_\varphi(T_{\mathrm{CMB}})}{f_\varphi(T_{\mathrm{CMB}}) + f_\nu(T_{\mathrm{CMB}})}\bigg|_{\mathrm{min}}\right] \simeq 0.4 \cdot 10^{-3} \frac{m_\varphi}{1\ \mathrm{GeV}} - 2.4 \tag{5.5}$$

Combining (5.3)–(5.5) we find that

$$\log_{10}\left[\sigma^{\varphi}_{\mathrm{DM-N}}\big|_{\mathrm{min}}\right] \simeq -43 + 0.4 \cdot 10^{-3} \frac{m_\varphi}{1\ \mathrm{GeV}} \tag{5.6}$$

where the constant is such that around $m_\varphi \sim 100$ GeV the scan points are above the XENON100 limit as shown in fig 12. The linearly growing part is a reminiscent of the m_φ dependence present in (5.5), as the mass dependence of $\lambda_{x\,\mathrm{min}}$ and m_φ in (5.4) cancel. Note however that the remaining mass dependence is very weak and in fact disappears after saturating (5.5) around 5 TeV, see figure 10.

Since there exist solutions in the resonance region it is important to calculate the Higgs-boson-decay branching ratio to $\varphi\varphi$, as those points could be excluded by measurements of the invisible Higgs-boson width. It turns out that for most of those solutions the $BR(h \to \varphi\varphi)$ is typically small and in agreement with the present data [49, 50]. It is worth noting that even though the XENON100 data excludes $\sigma_{\mathrm{DM-N}} \gtrsim 10^{-40} - 10^{-44}$ cm^2, other experiments, e.g. CREST-II [48], claim an observation of DM scattering with cross sections $\sigma_{\mathrm{DM-N}} \sim 10^{-40} - 5 \cdot 10^{-43}$ cm^2 (significantly above the XENON100 limits) and for DM mass range $10 - 60$ GeV. It is not our intention here to fit our model parameters to the CREST-II data, however few remarks are here in order. First, we have verified that our model could accommodate CREST-II 2σ data, though in that region of $\sigma^{\varphi}_{\mathrm{DM-N}}$,large λ_x is necessary; and since $m_\varphi < m_h/2$, the solutions that agree with CREST-II inevitably imply $BR(h \to \varphi\varphi) \sim 1$, which is in conflict with the present collider data. Note however that, since the CREST-II 2σ region is close to the threshold for $h \to \varphi\varphi$, therefore a modest ($\sim 3\sigma$) extension of the region towards the threshold allows us to find acceptable points

JHEP10(2013)158

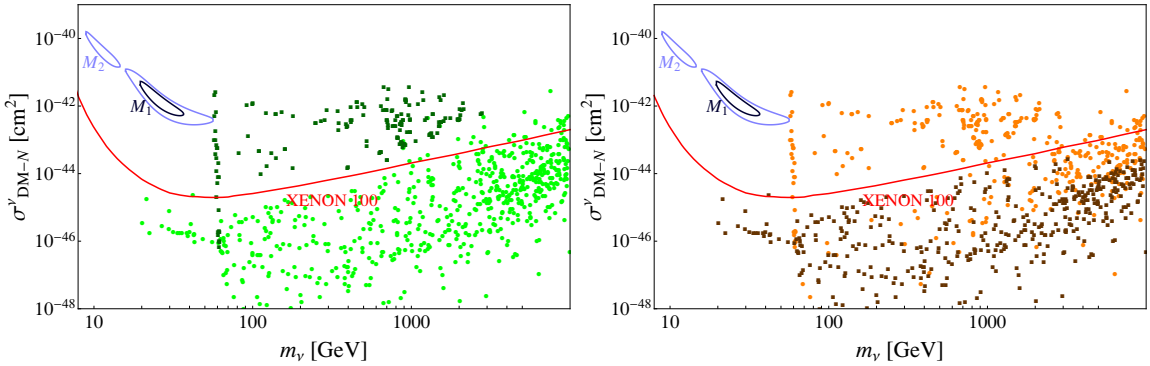

Figure 14. Plot of the cross section $\sigma^{\nu}_{\rm DM-N}$ as a function of ν for points satisfying the WMAP data within 3σ; the other parameters are randomly chosen in the ranges defined in the text (including both signs of λ_x). Left panel: green circles (dark green squares) correspond to case A (case B) solutions. Right panel: orange circles (dark orange squares) correspond to $\Omega_\varphi < \Omega_\nu$ ($\Omega_\varphi > \Omega_\nu$). The red line shows the XENON100 data, and the two islands in blue indicate 1 and 2σ CRESST-II results.

m_φ	65.82	66.73	66.94	67.05	67.08
m_ν	776	5373	654	85	4713
λ_x	0.18	0.1	0.11	0.11	0.11
g_ν	2.3	12.	9.6	8.5	11.
$\mathrm{Log}_{10}\sigma^{\varphi}_{DM-N}$	-42.3	-42.7	-42.6	-42.6	-42.6

Table 1. Points with $BR(h \to \varphi\varphi) = 0$ that satisfy WMAP bound within 3σ range and for which the cross section $\sigma^{\varphi}_{\rm DM-N}$ is within a 3σ range of the CREST-II region M_1 and with a m_φ that is not more than 10 GeV above the maximal (2σ) mass range for CREST-II.

above the threshold for which $BR(h \to \varphi\varphi) = 0$ since the decay is kinematically forbidden; a sample of those is shown in table 1. It is also worth noticing from the middle right panel of figure 7 that the corresponding Yukawa couplings could be smaller, $g_\nu \gtrsim 4$, than those that are needed to satisfy the XENON100 limit (red triangles) in the resonance region.

In figure 13 we illustrate temperature evolution of number densities (normalized such that at $T_{\rm CMB}$ they coincide with relict abundances) for a sample of points that are below XENON100 limit in figure 12.

As it has already been mentioned large abundance of dark neutrinos ν may imply that their contribution, although suppressed at the level of an amplitude, may be relevant after taking into account their relative number density:

$$\sigma^{\nu}_{\rm DM-N} = \frac{n_\nu}{n_\varphi + n_\nu}\sigma_{\nu N} \tag{5.7}$$

Results for the cross section $\sigma^{\nu}_{\rm DM-N}$ as a function of ν for points satisfying the WMAP are confronted with the XENON100 bound in figure 14. It is seen that the case A points are mostly in agreement with the bound, while the case B points leads to too large cross section. It is also worth to notice that points below the XENON100 limit correspond to $\Omega_\varphi > \Omega_\nu$ in agreement with our intuition.

JHEP10(2013)158

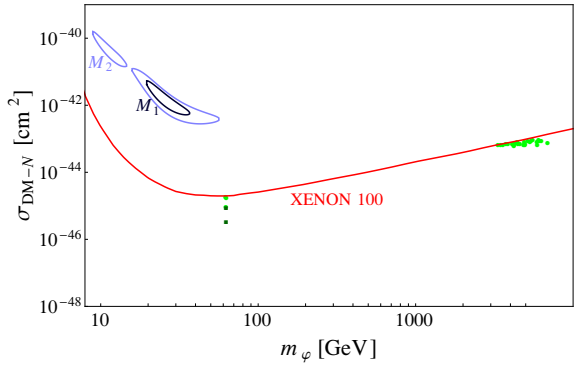

Figure 15. Plot of the cross section $\sigma_{\mathrm{DM-N}} = \sigma^{\varphi}_{\mathrm{DM-N}} + \sigma^{\nu}_{\mathrm{DM-N}}$ as a function of φ for points satisfying the WMAP data within 3σ; the other parameters are randomly chosen in the ranges defined in the text (including both signs of λ_x). Green circles (dark green squares) correspond to case A (case B) solutions. The red line shows the XENON100 data, and the two islands in blue indicate 1 and 2σ CRESST-II results.

So far we have been comparing separately φ and ν cross sections with experimental data. However one should take into account the fact that we do have *two component DM*. That is not quite straightforward if masses of the two components are different or their contributions are of the same order. Fortunately, it turns out that in almost all cases of interest it is meaningful to compare $\sigma_{\mathrm{DM-N}} \equiv \sigma^{\varphi}_{\mathrm{DM-N}} + \sigma^{\nu}_{\mathrm{DM-N}}$ with the experimental limits. The reason is that for all points of interest either φ and ν are almost degenerate, or the abundance is dominated by φ, and both these cases are well described by plotting $\sigma_{\mathrm{DM-N}}$ vs. m_φ. These results are presented in figure 15. The dark green squares stand for the case B points, so with , therefore in the first approximation we may compare $\sigma_{\mathrm{DM-N}}$ for those points with the limits. On the other hand, it turns out that light green circles correspond to points for which the cross section is dominated by scalars, so again those points might be compared with single-component DM limits.

6 Conclusions

We have discussed the main features of a two-component cold Dark Matter model composed of a neutral Majorana fermion (ν) and a neutral real singlet (φ). The Boltzmann equations for number densities of ν and φ were solved numerically and, for the case $m_\nu > m_\varphi$, an approximate analytical solution for the present DM abundance of both components was found. In order to determine a region of parameter space that is consistent both with WMAP and XENON100 data a scan over 4-dim parameter space was performed.

It has been shown that the agreement with the WMAP data requires that neutrinos cannot be substantially lighter than scalars, i.e. consistent solutions are found only for $m_\nu \gtrsim m_\varphi$. In the region where $m_\nu \simeq m_\varphi$ we observe interesting and strong implications of the presence (and interactions) of *two components* of DM, in particular, the thermal evolution of their number densities could be dramatically altered.

It has been shown that in a majority of the parameter space ν constitute the dominant component of the present energy density of DM. This observation agrees with a naive

JHEP10(2013)158

intuition: since ν's do not interact with the SM directly therefore they annihilate slower than φ's that couple directly to Higgs bosons. In order to enhance the annihilation rate for ν, large values of the $\nu - \varphi$ coupling $g_\nu \simeq 1 - 12$ are favored by the WMAP data. One could safely generalize the above observations and conclude that in the multi-component DM models the generic difficulty is an overabundance of the DM components that have no direct couplings to the SM. Another remark is that when the scalars φ are relatively heavy ($100 \lesssim m_\varphi \lesssim 1000$ GeV) their annihilation rate into SM particles must be amplified in order to maintain agreement with the WMAP data, that implies the Higgs portal ($\propto H^\dagger H \varphi^2$) coupling λ_x must grow with m_φ.

The XENON100 upper limit in DM-nucleon cross section, $\sigma_{\mathrm{DM-N}}$, turns out to be a very restrictive condition on the model. Let's first focus on the case with $\sigma_{\mathrm{DM-N}}$ dominated by the φ-N scattering. Naively one could expect that the prediction for $\sigma^{\varphi}_{\mathrm{DM-N}}$ could be reduced below the XENON100 limit by increasing m_φ. However there exist two obstacles that prohibit suppression of $\sigma^{\varphi}_{\mathrm{DM-N}}$ by enlarging the scalar mass (in the range $m_\varphi \gtrsim 100$ GeV): *(i)* in order to meet the WMAP constraint data on the present DM abundance the minimal value of the Higgs portal coupling constant λ_x must grow rapidly with m_φ, and *(ii)* the minimal relative scalar density $f_\varphi(T_{\mathrm{CMB}})/[f_\varphi(T_{\mathrm{CMB}}) + f_\nu(T_{\mathrm{CMB}})]$ also increases rapidly with m_φ. The two factors imply that the WMAP constraint restrict parameters to those for which $\sigma^{\varphi}_{\mathrm{DM-N}}$ is a approximately a constant function of m_φ; in particular, a large m_φ does not help to suppress $\sigma^{\varphi}_{\mathrm{DM-N}}$. Nevertheless for $m_\varphi \gtrsim 3$ TeV $\sigma^{\varphi}_{\mathrm{DM-N}}$ starts to be consistent with the XENON100 data since the bound becomes weaker at large m_φ. For those points $\Omega_\varphi > \Omega_\nu$. We have also found consistent solutions for $m_\varphi \simeq m_h/2$ and $m_\varphi \simeq 130 - 140$ GeV corresponding to $\Omega_\varphi < \Omega_\nu$.

The ν-DM cross section, $\sigma^{\nu}_{\mathrm{DM-N}}$, that appears at the 1-loop level was also calculated and its contribution was confronted with the XENON100 data. It has been shown that in the case A ($m_\nu > m_\varphi$) points that satisfy the WMAP constraint are mostly in agreement with the XENON100 bound, while in the case B ($m_\nu < m_\varphi$) the cross section is usually too large. It is also worth to notice that points below the XENON100 limit correspond to $\Omega_\varphi > \Omega_\nu$.

When both ν-N and φ-N cross sections are taken into account, it turns out only solutions with $m_\varphi \simeq m_h/2$ and $m_\varphi \gtrsim 3$ TeV survive.

It has been noticed that, since the CREST-II 2σ region is close to the threshold for $h \to \varphi\varphi$, therefore a moderate ($\sim 3\sigma$) extension of the region towards the $h \to \varphi\varphi$ threshold allowed us to find points consistent with the WMAP data with vanishing invisible decay width.

As a final remark we note that such a model is difficult to test at the Large Hadron Collider (LHC). The leading new effect would be production of scalar DM pairs, with a signature of missing energy associated with one or more jets. Such an analyses lie beyond the scope of this work.

JHEP10(2013)158

Acknowledgments

This work has been supported in part by the National Science Centre (Poland) as a research project, decision no DEC-2011/01/B/ST2/00438 and by the Foundation for Polish Science International PhD Projects Programme co-financed by the EU European Regional Development Fund. The work of SB is supported by the U.S. Department of Energy under Grant No. DE-SC0008541.

JHEP10(2013)158

A Dark matter annihilation

The diagrams contributing to the scalar $\varphi\varphi$ annihilation into SM particles are shown in figure 16. The corresponding cross sections are available in the literature(e.g. [51] and [52]); we have verified the results of [52]:

$$\begin{aligned}
\hat{\sigma}_{WW}(s) &= \frac{\lambda_x^2}{2\pi}\sqrt{1-\frac{4M_W^2}{s}}\frac{s^2}{(s-m_h^2)^2+m_h^2\Gamma_h^2}\left(\frac{12M_W^4}{s^2}-\frac{4M_W^2}{s}+1\right)\\
\hat{\sigma}_{ZZ}(s) &= \frac{\lambda_x^2}{4\pi}\sqrt{1-\frac{4M_Z^2}{s}}\frac{s^2}{(s-m_h^2)^2+m_h^2\Gamma_h^2}\left(\frac{12M_Z^4}{s^2}-\frac{4M_Z^2}{s}+1\right)\\
\hat{\sigma}_{\bar{f}f}(s) &= \frac{\lambda_x^2}{\pi}\left(\sqrt{1-\frac{4m_f^2}{s}}\right)^3\frac{m_f^2\,s}{(s-m_h^2)^2+m_h^2\Gamma_h^2}\\
\hat{\sigma}_{hh}(s) &= \frac{\lambda_x^2}{4\pi}\sqrt{1-\frac{4m_h^2}{s}}\left(\frac{(s+2m_h^2)^2}{(s-m_h^2)^2}+\frac{32v^4\lambda_x^2}{(s-2m_h^2)^2}\left(\frac{1}{1-\xi^2}+F(\xi)\right)-\frac{16v^2\lambda_x(s+2m_h^2)}{(s-2m_h^2)(s-m_h^2)}F(\xi)\right)
\end{aligned} \tag{A.1}$$

where $F(\xi)=\mathrm{ArcTanh}(\xi)/\xi$, $\xi=\sqrt{(s-4m_h^2)(s-4m_\varphi^2)}/(s-2m_h^2)$. The total cross section is then

$$\hat{\sigma}_{\varphi\varphi\to \mathrm{SM\,SM}}(s)=\hat{\sigma}_{WW}(s)+\hat{\sigma}_{ZZ}(s)+\sum_f\hat{\sigma}_{\bar{f}f}(s)+\hat{\sigma}_{hh}(s) \tag{A.2}$$

where the sum runs over all fermions f. The remaining DM↔DM cross sections are

$$\begin{aligned}
\hat{\sigma}_{\varphi\varphi\to\nu\nu}(s) &= \int d\Pi_\nu d\Pi'_\nu |M_{\varphi\varphi\nu\nu}|^2(2\pi)^4\delta^4(P-p_\nu-p'_\nu)\\
\hat{\sigma}_{\nu\nu\to\varphi\varphi}(s) &= \int d\Pi_\varphi d\Pi'_\varphi |M_{\varphi\varphi\nu\nu}|^2(2\pi)^4\delta^4(P-p_\varphi-p'_\varphi)
\end{aligned} \tag{A.3}$$

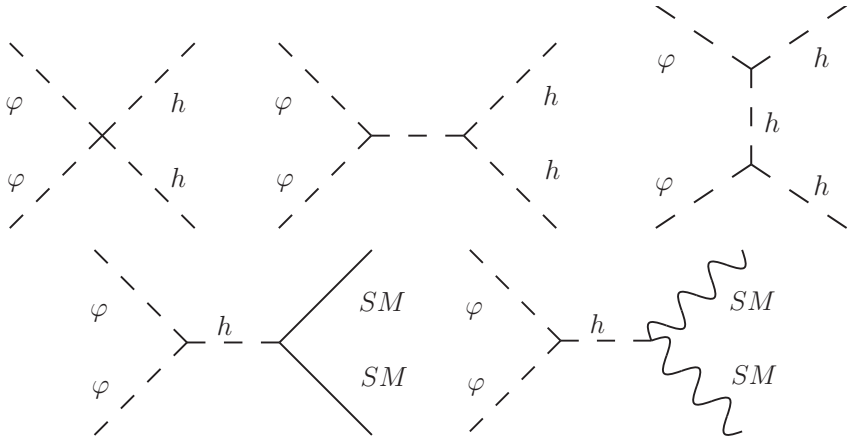

Figure 16. Diagrams contributing to the scalar $\varphi\varphi$ annihilation into SM particles.

where $d\Pi_X = \zeta_X d^3p_X/[(2\pi)^3 2E_X]$, P is the incoming momenta and the matrix element is given by

$$|M_{\varphi\varphi\nu\nu}|^2(s) = -\frac{g^4\left(4m_\nu^2 - s\right)A(s)}{2B(s)^2C(s)^2} \tag{A.4}$$

$$\begin{aligned}
A(s) = {} & 64(2(m_\nu - M_h)^2(m_\nu + M_h)^4 + 4(m_\nu - M_h)M_h(m_\nu + M_h)^2 m_\varphi^2 + (m_\nu^2 + 2M_v)^2 m_\varphi^4) \\
& 16(4(m_\nu - M_h)(m_\nu + M_h)^2(m_\nu + 2M_h) + 2(m_\nu^2 + 2m_\nu M_h + 4M_h^2)m_\varphi^2 - m_\varphi^4)s \\
& + 4\left(3m_\nu^2 + 8m_\nu M_h + 8M_h^2 - 2m_\varphi^2\right)s^2 + s^3 + \left(4m_\nu^2 - s\right)\left(-4m_\varphi^2 + s\right)^2 \mathrm{Cos}4\theta \\
& - 16m_\nu^2(4m_\varphi^2 - s)(4(m_\nu - M_h)(m_\nu + M_h)^2 + 4M_h m_\varphi^2 - (m_\nu + 2M_h)s)\mathrm{Cos}2\theta \\
B(s) = {} & \left(2m_\nu^2 - 2M_h^2 + 2m_\varphi^2 - s + \sqrt{-4m_\nu^2 + s}\sqrt{-4m_\varphi^2 + s}\mathrm{Cos}[\theta]\right) \\
C(s) = {} & \left(-2m_\nu^2 + 2M_h^2 - 2m_\varphi^2 + s + \sqrt{-4m_\nu^2 + s}\sqrt{-4m_\varphi^2 + s}\mathrm{Cos}[\theta]\right)
\end{aligned}$$

When $m_h > 2m_\varphi$ the decay $h \to \varphi\varphi$ is allowed and one has to modify the h width accordingly:

$$\Gamma_h = \Gamma_{h\to SM} + \Gamma_{h\to\varphi\varphi} \tag{A.5}$$

$$\Gamma_{h\to\varphi\varphi} = \frac{v^2\lambda_x^2}{8\pi m_h^2}\sqrt{m_h^2 - 4m_\varphi^2}\,\theta_H(m_h - 2m_\varphi) \tag{A.6}$$

where θ_H is the Heaviside step function (we also ignore 1-loop corrections to Γ_h that might include a contribution from $h \to \nu_h\nu_h$).

B Neutrino scattering

The diagram for neutrino scattering off a nucleon at 1-loop level is shown in figure 18. The amplitude modulus squared for a scattering $\nu q \to \nu q$ is the following:

$$|M_{\nu\nu qq}|^2 = \left(\frac{g_\nu^2\lambda_x m_q}{32\pi^2 M_h}\right)\left(\frac{\xi(m_\nu/M_h, m_\varphi/M_h, \sqrt{t}/M_h)}{t - m_h^2}\right)\left(4m_\nu^2 - t\right)\left(4m_q^2 - t\right) \tag{B.1}$$

JHEP10(2013)158

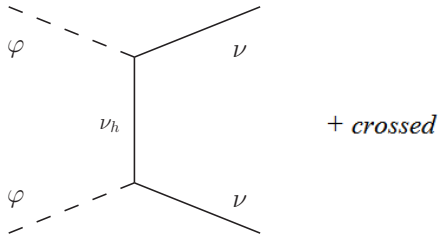

Figure 17. Diagrams contributing to the scalar $\varphi\varphi$ annihilation into DM neutrinos.

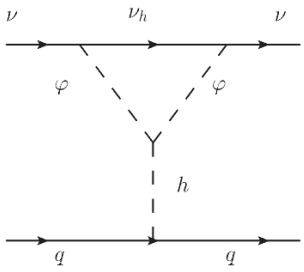

Figure 18. Diagram of the neutrino $\nu\nu$ scattering off a nucleon.

where

$$\xi(a,b,c) = \int_0^1 dz \frac{z(1+az)}{1-z-z(1-z)a^2+zb^2-z^2u(1-u)tc^2} \tag{B.2}$$

We are interested at the cross section at zero momentum transfer

$$\sigma_{\nu N} = \int_0^{4\mu^2 w^2} \frac{d\sigma(t=0)}{dt} dt = \frac{\mu^2}{\pi}\left(\frac{g_\nu^2 \lambda_x \xi(m_\nu/M_h, m_\varphi/M_h) m_N F}{32\pi^2 M_h m_h^2}\right) \tag{B.3}$$

where w is the relative velocity of dark matter to the nucleon, $F = \left(\sum_q f_q^N\right)$ (see [53]) and μ is defined as in (5.1).

References

[1] G. Bertone, D. Hooper and J. Silk, *Particle dark matter: Evidence, candidates and constraints*, *Phys. Rept.* **405** (2005) 279 [hep-ph/0404175] [INSPIRE].

[2] G. Bertone, *Particle Dark Matter*, Cambridge University Press, Cambridge U.K. (2010).

[3] M. Markevitch et al., *Direct constraints on the dark matter self-interaction cross-section from the merging galaxy cluster 1E0657-56*, *Astrophys. J.* **606** (2004) 819 [astro-ph/0309303] [INSPIRE].

[4] G.R. Blumenthal, S. Faber, J.R. Primack and M.J. Rees, *Formation of Galaxies and Large Scale Structure with Cold Dark Matter*, *Nature* **311** (1984) 517 [INSPIRE].

JHEP10(2013)158

[5] A. Klypin, J. Holtzman, J. Primack and E. Regos, *Structure formation with cold plus hot dark matter*, *Astrophys. J.* **416** (1993) 1 [astro-ph/9305011] [INSPIRE].

[6] W. Hu, *Structure formation with generalized dark matter*, *Astrophys. J.* **506** (1998) 485 [astro-ph/9801234] [INSPIRE].

[7] M.G. Abadi, J.F. Navarro, M. Steinmetz and V.R. Eke, *Simulations of galaxy formation in a lambda CDM universe. 2. The fine structure of simulated galactic disks*, *Astrophys. J.* **597** (2003) 21 [astro-ph/0212282] [INSPIRE].

[8] WMAP collaboration, G. Hinshaw et al., *Nine-Year Wilkinson Microwave Anisotropy Probe (WMAP) Observations: Cosmological Parameter Results*, *Astrophys. J. Suppl.* **208** (2013) 19 [arXiv:1212.5226] [INSPIRE].

[9] L. Bergstrom, *Nonbaryonic dark matter: Observational evidence and detection methods*, *Rept. Prog. Phys.* **63** (2000) 793 [hep-ph/0002126] [INSPIRE].

[10] S. Profumo, K. Sigurdson and L. Ubaldi, *Can we discover multi-component WIMP dark matter?*, *JCAP* **12** (2009) 016 [arXiv:0907.4374] [INSPIRE].

[11] G.B. Gelmini, *Dark matter searches: Looking for the cake or its frosting? Detectability of a subdominant component of the CDM*, *Nucl. Phys. Proc. Suppl.* **138** (2005) 32 [hep-ph/0310022] [INSPIRE].

[12] G. Duda, G. Gelmini, P. Gondolo, J. Edsjo and J. Silk, *Indirect detection of a subdominant density component of cold dark matter*, *Phys. Rev.* **D 67** (2003) 023505 [hep-ph/0209266] [INSPIRE].

[13] G. Duda, G. Gelmini and P. Gondolo, *Detection of a subdominant density component of cold dark matter*, *Phys. Lett.* **B 529** (2002) 187 [hep-ph/0102200] [INSPIRE].

[14] A. Drozd, B. Grzadkowski and J. Wudka, *Multi-Scalar-Singlet Extension of the Standard Model - the Case for Dark Matter and an Invisible Higgs Boson*, *JHEP* **04** (2012) 006 [arXiv:1112.2582] [INSPIRE].

[15] Q.-H. Cao, E. Ma, J. Wudka and C.-P. Yuan, *Multipartite dark matter*, arXiv:0711.3881 [INSPIRE].

[16] D. Feldman, Z. Liu, P. Nath and G. Peim, *Multicomponent Dark Matter in Supersymmetric Hidden Sector Extensions*, *Phys. Rev.* **D 81** (2010) 095017 [arXiv:1004.0649] [INSPIRE].

[17] M. Aoki, M. Duerr, J. Kubo and H. Takano, *Multi-Component Dark Matter Systems and Their Observation Prospects*, *Phys. Rev.* **D 86** (2012) 076015 [arXiv:1207.3318] [INSPIRE].

[18] J. Heeck and H. Zhang, *Exotic Charges, Multicomponent Dark Matter and Light Sterile Neutrinos*, *JHEP* **05** (2013) 164 [arXiv:1211.0538] [INSPIRE].

[19] K.M. Zurek, *Multi-Component Dark Matter*, *Phys. Rev.* **D 79** (2009) 115002 [arXiv:0811.4429] [INSPIRE].

[20] Y. Tomozawa, *Two components of dark matter in the DAMA data*, *Int. J. Mod. Phys.* **A 23** (2008) 4811 [arXiv:0806.1501] [INSPIRE].

[21] M. Malekjani, S. Rahvar and D. Jassur, *Two Component Baryonic-Dark Matter Structure Formation in Top-Hat Model*, *New Astron.* **14** (2009) 398 [arXiv:0706.3773] [INSPIRE].

[22] J.-H. Huh, J.E. Kim and B. Kyae, *Two dark matter components in dark matter extension of the minimal supersymmetric standard model and the high energy positron spectrum in PAMELA/HEAT data*, *Phys. Rev.* **D 79** (2009) 063529 [arXiv:0809.2601] [INSPIRE].

JHEP10(2013)158

[23] Y. Daikoku, H. Okada and T. Toma, *Two Component Dark Matters in $S_4 \times Z_2$ Flavor Symmetric Extra U(1) Model*, *Prog. Theor. Phys.* **126** (2011) 855 [arXiv:1106.4717] [INSPIRE].

[24] M. Aoki, J. Kubo and H. Takano, *Two-loop radiative seesaw with multicomponent dark matter explaining the possible gamma excess in the Higgs boson decay and at the Fermi LAT*, *Phys. Rev.* **D 87** (2013) 116001 [arXiv:1302.3936] [INSPIRE].

[25] A. Biswas, D. Majumdar, A. Sil and P. Bhattacharjee, *Two Component Dark Matter : A Possible Explanation of 130 GeV $\gamma-$ Ray Line from the Galactic Centre*, arXiv:1301.3668 [INSPIRE].

[26] P.-H. Gu, *Multi-component dark matter with magnetic moments for Fermi-LAT gamma-ray line*, *Phys. Dark Univ.* **2** (2013) 35 [arXiv:1301.4368] [INSPIRE].

[27] M. Cirelli and J.M. Cline, *Can multistate dark matter annihilation explain the high-energy cosmic ray lepton anomalies?*, *Phys. Rev.* **D 82** (2010) 023503 [arXiv:1005.1779] [INSPIRE].

[28] L. Bian, R. Ding and B. Zhu, *Two Component Higgs-Portal Dark Matter*, arXiv:1308.3851 [INSPIRE].

[29] M. Heikinheimo, A. Racioppi, M. Raidal, C. Spethmann and K. Tuominen, *Dark Supersymmetry*, *Nucl. Phys.* **B 876** (2013) 201 [arXiv:1305.4182] [INSPIRE].

[30] Z. Berezhiani and M.Y. Khlopov, *Physics of cosmological dark matter in the theory of broken family symmetry* (In Russian), *Sov. J. Nucl. Phys.* **52** (1990) 60 [INSPIRE].

[31] Y. Kajiyama, H. Okada and T. Toma, *Multicomponent dark matter particles in a two-loop neutrino model*, *Phys. Rev.* **D 88** (2013) 015029 [arXiv:1303.7356] [INSPIRE].

[32] P.T. Winslow, K. Sigurdson and J.N. Ng, *Multi-State Dark Matter from Spherical Extra Dimensions*, *Phys. Rev.* **D 82** (2010) 023512 [arXiv:1005.3013] [INSPIRE].

[33] K.R. Dienes and B. Thomas, *Dynamical Dark Matter: I. Theoretical Overview*, *Phys. Rev.* **D 85** (2012) 083523 [arXiv:1106.4546] [INSPIRE].

[34] K.R. Dienes and B. Thomas, *Dynamical Dark Matter: II. An Explicit Model*, *Phys. Rev.* **D 85** (2012) 083524 [arXiv:1107.0721] [INSPIRE].

[35] M.V. Medvedev, *Cosmological Simulations of Multi-Component Cold Dark Matter*, arXiv:1305.1307 [INSPIRE].

[36] V. Semenov, S. Pilipenko, A. Doroshkevich, V. Lukash and E. Mikheeva, *Dark matter halo formation in the multicomponent dark matter models*, arXiv:1306.3210 [INSPIRE].

[37] A. Kundu and S. Raychaudhuri, *Taming the scalar mass problem with a singlet Higgs boson*, *Phys. Rev.* **D 53** (1996) 4042 [hep-ph/9410291] [INSPIRE].

[38] B. Grzadkowski and J. Wudka, *Pragmatic approach to the little hierarchy problem: the case for Dark Matter and neutrino physics*, *Phys. Rev. Lett.* **103** (2009) 091802 [arXiv:0902.0628] [INSPIRE].

[39] B. Grzadkowski and J. Wudka, *Naive solution of the little hierarchy problem and its physical consequences*, *Acta Phys. Polon.* **B 40** (2009) 3007 [arXiv:0910.4829] [INSPIRE].

[40] I. Chakraborty and A. Kundu, *Controlling the fine-tuning problem with singlet scalar dark matter*, *Phys. Rev.* **D 87** (2013) 055015 [arXiv:1212.0394] [INSPIRE].

[41] A. Drozd, *RGE and the Fine-Tuning Problem*, arXiv:1202.0195 [INSPIRE].

JHEP10(2013)158

[42] M. Gonderinger, Y. Li, H. Patel and M.J. Ramsey-Musolf, *Vacuum Stability, Perturbativity and Scalar Singlet Dark Matter*, *JHEP* **01** (2010) 053 [arXiv:0910.3167] [INSPIRE].

[43] G. Cynolter, E. Lendvai and G. Pocsik, *Note on unitarity constraints in a model for a singlet scalar dark matter candidate*, *Acta Phys. Polon.* **B 36** (2005) 827 [hep-ph/0410102] [INSPIRE].

[44] M. Srednicki, R. Watkins and K.A. Olive, *Calculations of Relic Densities in the Early Universe*, *Nucl. Phys.* **B 310** (1988) 693 [INSPIRE].

[45] E. Kolb and M. Turner, *The Early Universe*, Westview Press (1994).

[46] P. Gondolo and G. Gelmini, *Cosmic abundances of stable particles: Improved analysis*, *Nucl. Phys.* **B 360** (1991) 145 [INSPIRE].

[47] XENON100 collaboration, E. Aprile et al., *Dark Matter Results from 225 Live Days of XENON100 Data*, *Phys. Rev. Lett.* **109** (2012) 181301 [arXiv:1207.5988] [INSPIRE].

[48] G. Angloher et al., *Results from 730 kg days of the CRESST-II Dark Matter Search*, *Eur. Phys. J.* **C 72** (2012) 1971 [arXiv:1109.0702] [INSPIRE].

[49] J.R. Espinosa, M. Muhlleitner, C. Grojean and M. Trott, *Probing for Invisible Higgs Decays with Global Fits*, *JHEP* **09** (2012) 126 [arXiv:1205.6790] [INSPIRE].

[50] Y. Bai, P. Draper and J. Shelton, *Measuring the Invisible Higgs Width at the 7 and 8 TeV LHC*, *JHEP* **07** (2012) 192 [arXiv:1112.4496] [INSPIRE].

[51] C. Burgess, M. Pospelov and T. ter Veldhuis, *The Minimal model of nonbaryonic dark matter: A Singlet scalar*, *Nucl. Phys.* **B 619** (2001) 709 [hep-ph/0011335] [INSPIRE].

[52] W.-L. Guo and Y.-L. Wu, *The Real singlet scalar dark matter model*, *JHEP* **10** (2010) 083 [arXiv:1006.2518] [INSPIRE].

[53] G. Bélanger, F. Boudjema, A. Pukhov and A. Semenov, *Dark matter direct detection rate in a generic model with MicrOMEGAs 2.2*, *Comput. Phys. Commun.* **180** (2009) 747 [arXiv:0803.2360] [INSPIRE].

JHEP10(2013)158